Monthly Notices of the ROYAL ASTRONOMICAL SOCIETY

MNRAS **543,** 1556–1573 (2025) https://doi.org/10.1093/mnras/staf1571
Advance Access publication 2025 September 16

Testing the local supervoid solution to the Hubble tension with direct distance tracers

Richard Stiskalek [1,2★] Harry Desmond [3] and Indranil Banik [3]

[1]*Department of Astrophysics, University of Oxford, Denys Wilkinson Building, Keble Road, Oxford OX1 3RH, UK*
[2]*Center for Computational Astrophysics, Flatiron Institute, 162 5th Ave, New York, NY 10010, USA*
[3]*Institute of Cosmology and Gravitation, University of Portsmouth, Dennis Sciama Building, Burnaby Road, Portsmouth PO1 3FX, UK*

Accepted 2025 September 13. Received 2025 August 29; in original form 2025 July 23

ABSTRACT

Several observational studies suggest that the local few hundred Mpc around the Local Group is significantly underdense based on source number counts in redshift space across much of the electromagnetic spectrum, particularly in near-infrared galaxy counts. This 'Keenan–Barger–Cowie (KBC) void', 'Local Hole', or 'local supervoid' would have significant ramifications for the Hubble tension by generating outflows that masquerade as an enhanced local expansion rate. We evaluate models for the KBC void capable of resolving the Hubble tension with a background *Planck* cosmology. We fit these models to direct distances from the Tully–Fisher catalogue of the CosmicFlows-4 compilation using a field-level forward model. Depending on the adopted void density profile, we find the derived velocity fields prefer a void size $\lesssim 70$ Mpc, which is $\lesssim 10$ per cent of the fiducial size found by Haslbauer et al. based on the KBC luminosity density data. The predicted local Hubble constant is $72.1^{+0.9}_{-0.8}$, $70.4^{+0.4}_{-0.4}$, or $70.2^{+0.5}_{-0.4}$ km s^{-1} Mpc^{-1} for an initial underdensity profile that is exponential, Gaussian, or Maxwell–Boltzmann, respectively. The latter two ameliorate the Hubble tension to within 3σ of the four-anchor distance ladder approach of Breuval et al., which gives 73.2 ± 0.9 km s^{-1} Mpc^{-1}. The exponential profile achieves consistency with this measurement at just over 1σ, but it is disfavoured by the Bayesian evidence. The preferred models produce bulk flow curves that disagree with recent estimates from CosmicFlows-4, despite the void models being flexible enough to match such estimates.

Key words: gravitation – methods: numerical – galaxies: distances and redshifts – galaxies: statistics – distance scale – large-scale structure of Universe.

1 INTRODUCTION

One of the biggest current puzzles in cosmology is the Hubble tension, a statistically significant discrepancy between the rate at which redshift increases with distance as inferred from the local distance ladder and the predicted rate assuming the Lambda cold dark matter (ΛCDM) model with parameters calibrated using the cosmic microwave background (CMB) anisotropies. In a homogeneously expanding universe, the redshift gradient $z' \equiv \mathrm{d}z/\mathrm{d}r$ with respect to distance r arises purely from cosmic expansion, implying that $cz' = \dot{a}$, where c is the speed of light, a is the cosmic scale factor, and an overdot denotes a time derivative (for a more detailed derivation, see the introduction to Mazurenko, Banik & Kroupa 2025). The expansion rate is quantified by the Hubble parameter $H \equiv \dot{a}/a$, leading to $cz' = H_0$ at the present day when $a \equiv 1$ (a subscript 0 denotes evaluation at $z = 0$). Since the overall expansion history $a(t)$ as a function of time t since the big bang can be predicted in ΛCDM, it is then possible to predict the local cz' using a calibration at early times based on the CMB anisotropies. The most precise such results are derived from the *Planck* mission (The Planck Collaboration 2006) – $H_0^{\mathrm{Planck}} = 67.4 \pm 0.5$ km s^{-1} Mpc^{-1} (Planck Collaboration VI 2020b; Tristram et al. 2024) – with similar values obtained from ground-based telescopes (Calabrese et al. 2025; Camphuis et al. 2025; Ge et al. 2025). However, cz' measured from the local distance ladder is persistently higher (for a review, see Di Valentino, Melchiorri & Silk 2021). The most precise local measurement is $H_0^{\mathrm{local}} = 73.17 \pm 0.86$ km s^{-1} Mpc^{-1} (Breuval et al. 2024) from the SH0ES programme (Riess et al. 2021), derived by calibrating the absolute magnitude of Type Ia supernovae (SNe Ia) with the Cepheid period–luminosity relation (Leavitt & Pickering 1912) in four-anchor galaxies with trigonometric distances. This is in 6σ tension with the CMB value, but agrees with other methods of building the local distance ladder without Cepheids, SNe Ia, or both (Pesce et al. 2020; Scolnic & Vincenzi 2023; Bhardwaj et al. 2025; Jensen et al. 2025; Vogl et al. 2025).

It has been suggested that the Milky Way resides in a large local underdensity or void, which would violate the relation $cz' = \dot{a}$ by providing an additional contribution to z' from peculiar velocity and gravitational redshift due to our location on a potential hill (Keenan, Barger & Cowie 2016; Shanks, Hogarth & Metcalfe 2019a; Shanks et al. 2019b; Ding, Nakama & Wang 2020; Camarena et al. 2022; San Martín & Rubio 2023; Cai, Ding & Wang 2025). A local void was in fact proposed long before the Hubble tension based on galaxy number counts across the whole electromagnetic spectrum. The claims for the largest and deepest void come from galaxy number counts in

★ E-mail: richard.stiskalek@physics.ox.ac.uk

the near-infrared (Keenan, Barger & Cowie 2013): the 'Keenan–Barger–Cowie (KBC) void'. This led Haslbauer, Banik & Kroupa (2020; hereafter HBK20) to construct a semi-analytic model relating the KBC void to the Hubble tension. Accounting for excess redshift induced by the void, HBK20 argued that the KBC void is roughly 20 per cent underdense out to 300 Mpc and causes the local cz' to exceed $\dot{a}$ by 11 ± 2 per cent (see their equation 5). This could fully solve the Hubble tension while retaining the *Planck* cosmology at the background level, i.e. the present $\dot{a} = H_0^{\rm Planck}$ (see fig. 3 of Di Valentino et al. 2025).

An important result of HBK20 was that the observed size and depth of the KBC void are inconsistent with ΛCDM expectations at 6σ, regardless of the absolute distance scale. This is because the ΛCDM power spectrum cosmic variance on 300 Mpc scales is only 4.8 per cent in redshift space, but observations across 90 per cent of the sky and most (57–75 per cent) of the luminosity function suggest an underdensity of 46 ± 6 per cent (see the light blue point on fig. 11 of Keenan et al. 2013). The lack of sufficient structure in ΛCDM on the relevant scales prevents it from solving the Hubble tension through cosmic variance (Wu & Huterer 2017), which is expected to be only ≈ 0.9 km s^{-1} Mpc^{-1} in the local cz' given the scales over which this is typically measured (Camarena & Marra 2018). As a result, a local void in the ΛCDM framework cannot solve the Hubble tension or explain the KBC void. However, if structure formation proceeded faster than expected in ΛCDM on scales $\gtrsim 100$ Mpc, cosmic variance might be enhanced sufficiently to solve both problems. The models of HBK20 were therefore based on Modified Newtonian dynamics (MOND; Milgrom 1983; Famaey & McGaugh 2012; Banik & Zhao 2022) as a convenient way to boost the gravitational field from a given density distribution; this is to be considered simply as a proxy for a theory with stronger gravity than ΛCDM. HBK20 considered initial underdensities at $z = 9$ ($a = 0.1$) conforming to exponential, Gaussian, and Maxwell–Boltzmann profiles, finding in each case the parameters that best fit the local redshift gradient and curvature from supernovae, the KBC void density profile inferred from galaxy number counts, strong lensing time delays, and the peculiar velocity of the Local Group (LG), which needs to be plausible given the predicted void velocity field. The models provided a satisfactory explanation for the observables, achieving an overall Gaussian-equivalent tension of 2.5σ, 2.8σ, and 2.9σ for the Maxwell–Boltzmann, Gaussian, and exponential profile, respectively.

The scope of the void model was extended in Mazurenko et al. (2024; hereafter M24) by fitting it to the bulk flow, a measure of the average velocity of galaxies within spheres of varying radii centred on our location (Watkins, Feldman & Hudson 2009; Feldman, Watkins & Hudson 2010; Nusser & Davis 2011; Hoffman, Courtois & Tully 2015; Watkins & Feldman 2015; Nusser 2016; Scrimgeour et al. 2016; Feix, Branchini & Nusser 2017; Hellwing, Bilicki & Libeskind 2018; Peery, Watkins & Feldman 2018). This was motivated by an inference of the bulk flow by Watkins et al. (2023; hereafter W23), which indicated tension with the ΛCDM expectation at the 5σ level. The bulk flow was measured using the CosmicFlows-4 (CF4) compilation of redshifts and redshift-independent distances (Tully et al. 2023), finding increasing tension out to 250 Mpc h^{-1}. The bulk flow magnitude claimed by W23 was later corroborated by Whitford, Howlett & Davis (2023), though they were only able to probe out to 173 Mpc h^{-1} due to a more conservative methodology. They also argued that the uncertainties in the bulk flow claimed by W23 were underestimated by a factor of ≈ 3.5. M24 showed that the void model calibrated in HBK20 can explain the anomalous CF4 bulk flow curve reported by W23, but this is based on a misunderstanding in M24, which alters their conclusions regarding the preferred void properties and our location in the void.[1] It is therefore important to revisit the issue of whether the local velocity field is consistent with the void model.

While our focus is at low z, an important consequence of a local void model is that we expect a return to the *Planck* cosmology at high z. The rate of convergence was explored in more detail by Mazurenko et al. (2025) in terms of $H_0(z)$, the value of H_0 that would be inferred using data in a narrow redshift range centred on z. They found good agreement with the observationally inferred $H_0(z)$ (Jia, Hu & Wang 2023; Jia et al. 2025). The expectation that high-redshift data sets are consistent with the *Planck* cosmology can be assessed using cosmic chronometers (CCs), which have very little sensitivity to $z \lesssim 0.3$ because the CC technique involves finding $\dot{z}$ by comparing the differential age between galaxy populations at two redshifts (Moresco 2024, and references therein). Results using CCs combined with other uncalibrated data sets lead to H_0 values very close to $H_0^{\rm Planck}$ and below the local cz' (Cogato et al. 2024; Guo et al. 2025). This is also the case with strong lensing time delays of supernova Refsdal (Kelly et al. 2023; Grillo et al. 2024). Moreover, the ages of the oldest Galactic stars are much more in line with the low $H_0^{\rm Planck}$ (Cimatti & Moresco 2023; Valcin et al. 2025; Xiang et al. 2025). For a summary of these and other constraints on H_0 and the matter density parameter $\Omega_{\rm m}$, we refer the reader to Banik & Samaras (2025).

The local void scenario was challenged by Kenworthy, Scolnic & Riess (2019) using the distance–redshift relation of SNe Ia. However those authors assumed that a local void would have essentially no effect on redshifts at $z > 0.1$ (see their fig. 1), which is not the case in the models of HBK20 (see fig. 3 of Mazurenko et al. 2025). It may also be relevant that SNe Ia are not standard candles, but merely standardizable (Phillips 1993; Tripp 1998; Brout et al. 2022). The standardization procedure can introduce dependence on the cosmological model (Lane et al. 2025), making it important to jointly infer the cosmological parameters with the calibration parameters (Seifert et al. 2025). This may cast doubt on studies that argue against a local void using SNe Ia while calibrating their Tripp parameters using a void-free model (Camarena et al. 2022; Castello, Högås & Mörtsell 2022). These issues can be avoided by using instead baryon acoustic oscillation (BAO) measurements over the last 20 yr, which show a preference for a local void (Banik & Kalaitzidis 2025) or other late-time adjustment to the *Planck* cosmology such as dynamical dark energy (DESI Collaboration 2025b), though the latter approach worsens the Hubble tension (Hamidreza Mirpoorian, Jedamzik & Pogosian 2025).

This work focuses on low z and extends the analysis of M24 by analysing velocities at the field-level (i.e. galaxy-by-galaxy), rather than relying solely on the reported bulk flow curve. The advantage of this is twofold. First, it lets us extract more information from the data without compressing them into a summary statistic. Secondly, it lets us avoid assumptions about the accuracy of the bulk flow produced by W23, including the accuracy of their error model (questioned by Whitford et al. 2023). Indeed, a field-level inference allows us to check the bulk flow estimate of W23 by investigating consistency between constraints on the void velocity field inferred by fitting to the W23 bulk flow versus fitting the galaxies individually and deriving the posterior predicted bulk flow from the latter. In particular, we use the Tully–Fisher relation (TFR; Tully & Fisher 1977) sample from

[1] This is acknowledged and rectified by all those authors in a subsequent study (Mazurenko et al., submitted).

the CF4 survey (Kourkchi et al. 2020a, b; Tully et al. 2023), deriving constraints on the void profile, size, the observer offset from the void centre, and the velocity with which the void moves with respect to the rest of the universe.

In Section 2, we explain the data we use and the quality cuts we apply. Our methods are described in Section 3. We then present our results in Section 4 and discuss them in Section 5. We conclude in Section 6. All logarithms in this work are base 10. We use the notation $\mathcal{N}(x; \mu, \sigma)$ to denote the normal distribution with mean μ and standard deviation σ evaluated at x.

2 OBSERVATIONAL DATA

The TFR is an empirical relation between the width W of a spectral line in a spiral galaxy (typically the 21 cm H I line of neutral hydrogen) as a measure of its rotation velocity, and absolute magnitude M as a measure of its luminosity (Tully & Fisher 1977). We write the relation as

$$M = \begin{cases} a_{\rm TFR} + b_{\rm TFR}\eta + c_{\rm TFR}\eta^2 & \text{if } \eta > 0, \\ a_{\rm TFR} + b_{\rm TFR}\eta & \text{otherwise,} \end{cases} \quad (1)$$

where $a_{\rm TFR}$, $b_{\rm TFR}$, and $c_{\rm TFR}$ are the zero-point, slope, and curvature, respectively. We reparametrize the linewidth by introducing a parameter η such that

$$\eta \equiv \log \frac{W}{\mathrm{km\,s^{-1}}} - 2.5. \quad (2)$$

From now on, we refer to η as the linewidth. In the subsequent analysis, we will jointly infer the TFR calibration parameters along with the intrinsic scatter $\sigma_{\rm TFR}$. Curvature is included at $\eta > 0$, where the relation is empirically found to deviate from linearity.

We use the CF4 TFR survey, which contains 9792 galaxies at $z < 0.065$, with 5027 in the Sloan Digital Sky Survey (SDSS) i-band subsample and 3278 in the Wide-field Infrared Survey Explorer (WISE) $W1$ subsample (Kourkchi et al. 2020a, b; Tully et al. 2023). We show the redshift distribution of the sample in Fig. 1. Our selection includes galaxies with $\eta > -0.3$, Galactic latitude $|b| > 7.5^\circ$, and a photometric quality flag of 5 (the best quality). The cut in η eliminates dwarf and low-mass galaxies, which are difficult to detect and may follow a different TFR or have higher scatter. In addition, their peculiar velocities are more strongly affected by non-linear motions (e.g. as satellites) and thus do not provide a reliable probe of the large-scale velocity field. The cut in b is to mask out sources close to the Galactic Zone of Avoidance. Lastly, we exclude 168 galaxies identified as TFR outliers by Boubel et al. (2024). We use the SDSS photometry when available and WISE otherwise. We assign distinct TFR parameters for each photometric system, since differences in photometry or calibration result in distinct TFRs. Following the selection, the joint sample contains 5025 and 2094 galaxies with SDSS and WISE photometry, respectively.

Furthermore, we adopt the Cepheid-based absolute calibration from the SH0ES catalogue (Riess et al. 2022). Out of the 40 galaxies with Cepheid-derived distances, we match 18 of them to the CF4 TFR catalogue, of which only 12 remain in the CF4 sample after applying the selection criteria described above. The consistency of the SH0ES Cepheid calibration has been recently investigated by Nájera & Desmond (2025), who found no evidence for unaccounted-for systematics. However, we emphasize that we do not infer the value of the Hubble constant directly – this is implicitly fixed to the *Planck* value, which defines the background cosmology used to construct the void model. Instead, the absolute calibration is used to break the degeneracy between a radial outflow induced by the void and a global zero-point offset in the Tully–Fisher normalization.

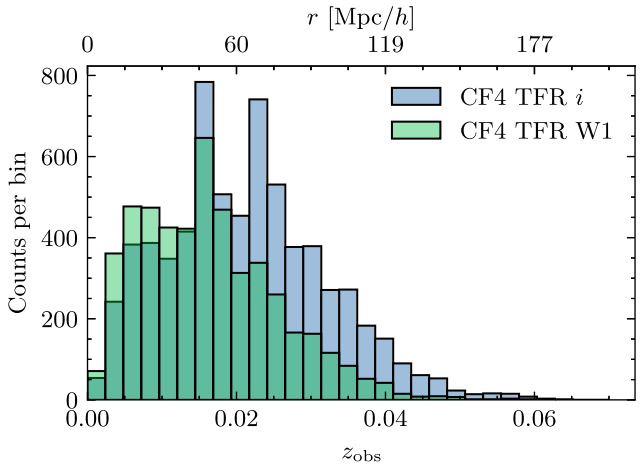

Figure 1. The distribution of galaxy redshifts in the CMB frame ($z_{\rm obs}$) for the CF4 TFR sample. The upper x-axis shows $z_{\rm obs}$ converted to comoving distance assuming no peculiar velocity. The plot shows separately the set of galaxies with i-band SDSS photometry and $W1$-band WISE photometry.

3 METHODOLOGY

Here we introduce our methodology to set constraints on the local void from the peculiar velocity data. The model of void growth is from HBK20, with fixed initial density contrast and variable parameters including the void's external velocity, void size, and observer position (Section 3.1). We first derive constraints based on the bulk flow curve, incorporating an important correction for projection effects that was previously neglected (Section 3.2). We then describe the main method of this paper: a full galaxy-by-galaxy Tully–Fisher flow model to jointly infer void and calibration parameters (Section 3.3). An additional constraint from the CMB quadrupole is described in Appendix A: the off-centre lensing contribution to large-scale anisotropies must remain subdominant, imposing an upper bound on the induced quadrupole amplitude ($a_{20} < 10^{-5}$), which significantly restricts the allowed void parameter space. These constraints are particularly relevant for the fiducial void size considered in HBK20, implying that the observer must lie within ≈ 90 Mpc of the void centre for all three profiles. However, the CMB quadrupole does not impose significant constraints on the smaller voids preferred by our field-level analysis.

3.1 Void model

The relation between the density contrast of a local void and the outflow it induces depends on the void's growth history. Standard equations cannot consistently describe this growth in the case of the KBC void because its properties are in 6.0σ tension with ΛCDM expectations, an issue that is observationally unrelated to the Hubble tension (section 2.2 of HBK20). In ΛCDM, accurate measurements of the CMB anisotropies provide a precise calibration of the early Universe density contrasts on the relevant scale of 300 comoving Mpc (cMpc), which in turn fixes the expected density fluctuations on that scale today. Since this expectation is contradicted by the observed density contrast of the KBC void, those authors were motivated to adopt a semi-analytic model with enhanced structure growth based

on the MOND framework (Milgrom 1983). This was used to evolve an initial density perturbation from $a = 0.1$ to the present epoch (see section 3.2 of HBK20).

Those authors considered three initial underdensity profiles: exponential, Gaussian, and Maxwell–Boltzmann. This was to allow exploration of how the density profile might impact the results. In the exponential and Gaussian profiles, the void is deepest at its centre, which is more in line with the observed density profiles of simulated and observed voids on smaller scales (Nadathur et al. 2015; Curtis, McDonough & Brainerd 2025). The Maxwell–Boltzmann profile has a density profile that climbs back to the cosmic mean value at the void centre, placing the deepest part of the void somewhat off-centre. This unusual arrangement appears not to work well with the bulk flow curve (M24), but is none the less considered here for completeness. It was originally considered in HBK20 based on the observations of Karachentsev & Telikova (2018), which suggest that the density within 11 Mpc is larger than the density within 40 Mpc, implying that the density first decreases away from us before then rising back up. However, the number of galaxies within 11 Mpc is quite small, making it unclear how reliable these results are. Moreover, there is an obvious anthropic selection effect in that we need to reside within a galaxy, implying that the average density on sufficiently small scales must rise, even if we are within a supervoid.

We model the growth history of the void using the same approach and fix the initial void density contrast to the best-fitting values in tables 4 and C1 of HBK20. However, we treat the systemic velocity of the void relative to the rest of the Universe ($\boldsymbol{V}_{\rm ext}$), the void size relative to its fiducial value ($\tilde{r}_{\rm void}$), and our offset from the void centre ($R_{\rm offset}$) as free parameters (HBK20 were unable to constrain the latter). The models considered are spherically symmetric outflow models, but the introduction of $\boldsymbol{V}_{\rm ext}$ reduces this symmetry to axisymmetry. To transform into the CMB frame, we apply an additional Galilean transformation. To avoid added complexity, we restrict our vantage point to positions along the void symmetry axis (similarly to M24).

The best-fitting initial void size from HBK20 is 1030 cMpc for both the exponential and Gaussian profiles, but only 228.2 cMpc for the Maxwell–Boltzmann profile (see their tables 4 and C1). To relax this assumption, we scale the void size relative to these values by $\tilde{r}_{\rm void}$, which we treat as a free parameter. Additionally, to mimic the effect of varying the void depth, we scale the void-predicted peculiar velocities by the factor β, which we sample.

3.2 Updated constraints from the bulk flow curve

An important constraint on the local void model is the predicted $\boldsymbol{V}_{\rm pec}$ of each observed galaxy with a redshift-independent distance. One way to describe the velocity field of the local Universe is to consider all galaxies within a sphere of radius R centred on our location and compute their average velocity. This is the bulk flow $\boldsymbol{V}_b$. Taking the average within a spherical region would in ideal circumstances completely eliminate dependence on the assumed H_0, whose value is highly controversial yet necessary to calculate an individual galaxy's peculiar velocity. Observationally, $\boldsymbol{V}_b$ must be calculated using only line-of-sight (LOS) peculiar velocities $V_{\rm pec}$. These can be treated as vectors pointing along the LOS, such that $\boldsymbol{V}_{\rm pec}^{\rm LOS} \equiv V_{\rm pec}\,\hat{\boldsymbol{r}}$, where $\hat{\boldsymbol{r}}$ is the unit vector towards the galaxy.

Recently, W23 measured the bulk flow curve $\boldsymbol{V}_b(R)$ out to 250 Mpc h^{-1}. This motivated M24 to compare their measurements to the predictions of the local void model. M24 discuss this procedure in their section 2.3, with their equation (4) stating that

$$\boldsymbol{V}_b = \frac{\sum_i w_i \boldsymbol{V}_{\rm pec}^{\rm LOS}}{\sum_i w_i}, \tag{3}$$

where w_i is the relative statistical weight assigned to the ith galaxy, which in the model corresponds to the volume of each cell. Since the void models considered by M24 were axisymmetric, it was clear that $\boldsymbol{V}_b$ would point along the symmetry axis, so only this component of $\boldsymbol{V}_{\rm pec}^{\rm LOS}$ had to be considered. The consideration of only one axis direction is motivated by all the observationally reported bulk flows from W23 being aligned with each other to within a few degrees. This common direction can be taken as the symmetry axis of the void model given the lack of any other constraints on how it should be oriented.

M24 pointed out that due to the need to project peculiar velocities on to the LOS and then on to the symmetry axis, $\boldsymbol{V}_b$ calculated in this way will be only $\boldsymbol{V}_{\rm pec}/3$ if all galaxies in the considered volume have the same $\boldsymbol{V}_{\rm pec}$. However, this approach is not how the bulk flow is defined in the literature. Indeed, equation (2) of Nusser (2016) recovers equation (3), but with an extra factor of 3. This is designed to mitigate the above-mentioned projection issues, so the estimated $\boldsymbol{V}_b = \boldsymbol{V}_{\rm pec}$ if $\boldsymbol{V}_{\rm pec}$ is the same for all galaxies, making the results much simpler to interpret. To illustrate the origin of the factor of 3, consider the relation between the constant bulk velocity $\boldsymbol{V}_b$ and its LOS projection for a top-hat filter, where the bulk flow is defined as the volume average of the LOS velocity treated as a vector pointing along the LOS.

$$\boldsymbol{V}_b = 3 \times \frac{1}{V} \int {\rm d}V\ (\boldsymbol{V}_b \cdot \hat{\boldsymbol{r}})\,\hat{\boldsymbol{r}}, \tag{4}$$

where V is the enclosed volume and ${\rm d}V$ is the volume element. This identity holds only when the factor of 3 is included, which is not the case in equation (3). As a result, *all the bulk flow predictions in M24 must be tripled* (as acknowledged by those authors in Mazurenko et al. submitted). The corrected formula is therefore

$$\boldsymbol{V}_b = \frac{3\sum_i w_i \boldsymbol{V}_{\rm pec}^{\rm LOS}}{\sum_i w_i}. \tag{5}$$

M24 did not vary the void model parameters and only considered a very limited number of possible vantage points. Given the bulk flow curves were found to be in good agreement with the measurements of W23, it is clear that tripling the model predictions to account for the above mistake would lead to a very poor agreement. To check if the local void scenario might still be plausible, in this work we explore a much wider range of model parameters, varying not only our vantage point but also the void external velocity $\boldsymbol{V}_{\rm ext}$ (Section 3.1). In each case, we compute the χ^2 as the minimum of χ^2_+ and χ^2_-, where

$$\chi^2_\pm = \sum_i \left(\frac{V_{b,i}^{\rm obs} \mp V_{b,i}^{\rm pred}}{\sigma\left(V_{b,i}^{\rm obs}\right)} \right)^2, \tag{6}$$

where the sum runs over the radial bins indexed by i. The model predictions and observations are distinguished using 'pred' and 'obs' superscripts, respectively, with the latter having an uncertainty of $\sigma\left(V_b^{\rm obs}\right)$. The two possible choices of sign arise because unlike the observed bulk flow curve where the directions are all very nearly parallel, the predicted bulk flow curve could reverse direction (this occurs for the outer vantage points in fig. 1 of M24). Since there is no a priori way to know if $\boldsymbol{V}_{\rm ext}$ is parallel to the observed $\boldsymbol{V}_b$ found by W23 or in the opposite direction, we can orient the void model as we wish. We therefore compute χ^2_+ and χ^2_- using both the predicted bulk flow curve $\boldsymbol{V}_b^{\rm pred}(R)$ and its negative $-\boldsymbol{V}_b^{\rm pred}(R)$,

respectively, and then find min $\left(\chi^2_+, \chi^2_-\right)$. We assume for simplicity that the measurements of W23 are all independent and yield the same direction. However, even if the bulk flow direction is constant, the independence assumption is clearly violated, as the bulk flow represents a cumulative measurement of the mean velocity within concentric spheres. This will introduce some systematic error into this part of the analysis. We also take advantage of the two extra points at low radii shown in fig. 1 of M24. It is clear that if there are model parameters that give an acceptable χ^2 in this sense, the parameters must be quite different to those considered by M24, so a successful fit can no longer be considered a successful a priori prediction of the model.

3.3 Object-by-object velocity field model

To extract more of the information contained in the direct-distance catalogues, we perform a galaxy-by-galaxy fit without first compressing the data into a bulk flow. We simultaneously calibrate the TFR and infer the parameters of the void model, which predicts both the density and the radial velocity. In the CMB frame, the total source redshift $z_{\rm CMB}$ is given by

$$1 + z_{\rm CMB} = (1 + z_{\rm cosmo})\left(1 + z_{\rm pec}\right), \tag{7}$$

where $z_{\rm cosmo} = a^{-1} - 1$ is the redshift due to cosmic expansion and $z_{\rm pec} = V_{\rm pec}/c$ is the redshift due to the radial peculiar velocity $V_{\rm pec}$, also measured in the CMB frame (see e.g. section 2.3 of Davis et al. 2019). We assume a flat ΛCDM universe dominated by non-relativistic matter and dark energy to convert between the cosmological redshift and the comoving distance (as described by, e.g. Hogg 1999),

$$r(z_{\rm cosmo}) = \frac{c}{H_0}\int_0^{z_{\rm cosmo}} \frac{{\rm d}z'}{\sqrt{\Omega_{\rm m}(1+z')^3 + (1-\Omega_{\rm m})}}, \tag{8}$$

where $\Omega_{\rm m}$ is the matter density parameter.[2] The peculiar velocity $V_{\rm pec}$ at the source position $\boldsymbol{r}$ is given by

$$V_{\rm pec} = \beta V_{\rm void}(\boldsymbol{r}) + \boldsymbol{V}_{\rm ext}\cdot\hat{\boldsymbol{r}}, \tag{9}$$

where $V_{\rm void}(\boldsymbol{r})$ denotes the radial velocity predicted by the void model at position $\boldsymbol{r}$ in the reference frame comoving with the void. In equation (9), we introduce β, a velocity scaling parameter that can either be treated as a free parameter or fixed to 1. By default, we treat it as a free parameter to mimic the effect of varying the void depth; it may also be interpreted simply as the average factor by which the model underpredicts or overpredicts outflow velocities.

The TFR relates the linewidth to the absolute magnitude M. Together with the apparent magnitude m, this determines the distance modulus μ as

$$\mu = m - M(\eta). \tag{10}$$

The distance modulus is expressed as a function of the luminosity distance $d_{\rm L}$:

$$\mu = 5\log\frac{d_{\rm L}}{\rm Mpc} + 25, \tag{11}$$

where the luminosity distance is related to the comoving distance r by $d_{\rm L} = (1 + z_{\rm cosmo})r$.

[2]This may introduce a mild internal inconsistency if the void model, which must be sourced by a cosmology with faster structure growth than ΛCDM, also modifies the background expansion.

We jointly infer the aforementioned void parameters and the distance indicator calibration, both collectively denoted as $\boldsymbol{\theta}$, along with the Bayesian evidence for each model. To achieve this, we use the TFR flow model of Stiskalek et al. (2025; hereafter S25), where we derive the likelihood of observing a galaxy with redshift $z_{\rm obs}$ (with uncertainty σ_{cz}/c) in the CMB frame, apparent magnitude $m_{\rm obs}$ (with uncertainty σ_m), and linewidth $\eta_{\rm obs}$ (with uncertainty σ_η), given the TFR calibration and an underlying density and velocity field. In our case, these are the fields predicted by the void model.

For each galaxy, we introduce three latent parameters: its 'true' comoving distance r, apparent magnitude $m_{\rm true}$ at this distance, and linewidth $\eta_{\rm true}$. All three are unknown and must be marginalized over. However, r can be numerically marginalized during each likelihood evaluation, rather than directly sampled. The parameters $m_{\rm true}$ and $\eta_{\rm true}$ are related to the observed values through selection functions $S(m_{\rm obs})$ for apparent magnitude and $S(\eta_{\rm obs})$ for linewidth, respectively, and the measurement uncertainties.

Together with the TFR calibration, $m_{\rm true}$ and $\eta_{\rm true}$ provide an estimate of the galaxy distance modulus:

$$\mu_{\rm TFR} = m_{\rm true} - \begin{cases} a_{\rm TFR} + b_{\rm TFR}\eta_{\rm true} + c_{\rm TFR}\eta_{\rm true}^2 & \text{if } \eta_{\rm true} > 0, \\ a_{\rm TFR} + b_{\rm TFR}\eta_{\rm true} & \text{otherwise.} \end{cases} \tag{12}$$

The TFR-based $\mu_{\rm TFR}$ is related to the true distance modulus $\mu_{\rm true}$ through the intrinsic scatter of the TFR and the homogeneous and inhomogeneous Malmquist biases. The homogeneous Malmquist bias is a simple r^2 volume factor in the prior on r, while the inhomogeneous Malmquist bias depends on the source number density $n(r)$. We assume that $n(r)$ is proportional to the matter density at the source position as predicted by the void model, such that $n(r) \propto \rho(r)$. In S25, we adopted a power-law bias of the form ρ^α, treating α as a free parameter. In the main analysis here, we instead fix $\alpha = 1$ for simplicity. Nevertheless, we verify that allowing α to vary, or adopting a linear bias model, does not significantly affect our results. In particular, the void size constraints, presented later, change by at most 1 per cent under these alternative bias assumptions. We use r to calculate the cosmological redshift (equation 8), which we combine with an estimate of the peculiar velocity at r from the void model, thereby obtaining the predicted redshift $z_{\rm pred}$ in the CMB frame (equation 7). σ_v is a Gaussian uncertainty between $cz_{\rm pred}$ and $cz_{\rm obs}$, assumed to be position-independent. σ_v captures the effect of small-scale motions that are not accounted for by the void model.

Thus, altogether the likelihood is as follows:

$$\begin{aligned}\mathcal{L}(z_{\rm obs},\, m_{\rm obs},\, \eta_{\rm obs}|\boldsymbol{\theta},\, m_{\rm true},\, \eta_{\rm true}) &= \int {\rm d}r\, \mathcal{N}\left(cz_{\rm obs}; cz_{\rm pred}, \sqrt{\sigma_v^2 + \sigma_{cz_{\rm obs}}^2}\right) \\ &\times \frac{r^2 n(r)\mathcal{N}\left(\mu_{\rm true}; \mu_{\rm TFR}, \sigma_{\rm TFR}\right)}{\int r'^2 n(r')\mathcal{N}\left(\mu'_{\rm true}; \mu_{\rm TFR}, \sigma_{\rm TFR}\right){\rm d}r'} \\ &\times \frac{S(m_{\rm obs})\mathcal{N}(m_{\rm obs}; m_{\rm true}, \sigma_m)}{\int S(m'_{\rm obs})\mathcal{N}(m'_{\rm obs}; m_{\rm true}, \sigma_m){\rm d}m'_{\rm obs}} \\ &\times \frac{S(\eta_{\rm obs})\mathcal{N}(\eta_{\rm obs}; \eta_{\rm true}, \sigma_\eta)}{\int S(\eta'_{\rm obs})\mathcal{N}(\eta'_{\rm obs}; \eta_{\rm true}, \sigma_\eta){\rm d}\eta'_{\rm true}}.\end{aligned} \tag{13}$$

Further details are provided in S25. We adopt the same apparent magnitude selection as S25, which is modelled following Boubel et al. (2024). Additionally, we assume that the selection in linewidth is a simple truncation, such that only values with $\eta_{\rm obs} > -0.3$ are observed. Assuming the galaxies are measured independently, the combined likelihood is given by the product of the likelihoods for individual galaxies.

Without additional information, the distribution of apparent magnitudes of sources at fixed absolute magnitude (or analogously $\eta_{\rm true}$)

Table 1. Summary of the free parameters of our galaxy-by-galaxy flow model and their priors.

Parameter	Description	Prior
Void parameters		
$R_{\rm offset}$	Local Group offset from the centre of the void	Uniform
$\tilde{r}_{\rm void}$	Void size relative to the estimate of HBK20	Uniform
Velocity field parameters		
$\boldsymbol{V}_{\rm ext}$	External velocity vector	Uniform in both magnitude and direction
σ_v	Scatter between the observed and predicted redshift	$\pi(\sigma_v) \propto 1/\sigma_v$
β	Velocity field scaling parameter	Uniform
TFR distance calibration parameters		
$a_{\rm TFR}$, $b_{\rm TFR}$, $c_{\rm TFR}$	TFR coefficients (zero-point, slope, and curvature)	Uniform
$\sigma_{\rm TFR}$	TFR magnitude intrinsic scatter	$\pi(\sigma_{\rm TFR}) \propto 1/\sigma_{\rm TFR}$
Galaxy latent parameters		
$m_{\rm true}$	Galaxy apparent magnitude	$p(m_{\rm true}\|\eta_{\rm true}, \boldsymbol{\theta}) \propto 10^{0.6\, m_{\rm true}}$
$\eta_{\rm true}$	True galaxy linewidth	$\mathcal{N}(\eta_{\rm true}\|\hat{\eta}, w_\eta)$
$\hat{\eta}$	Mean of the linewidth Gaussian hyperprior	Uniform
w_η	Standard deviation of the linewidth Gaussian hyperprior	$\pi(w_\eta) \propto 1/w_\eta$

is

$$p(m_{\rm true}|\eta_{\rm true}, \boldsymbol{\theta}) \propto 10^{0.6\, m_{\rm true}}. \tag{14}$$

This can be derived by assuming a uniform distribution of equal-magnitude objects with a radial distribution $\propto r^2$ in Euclidean space (Hubble 1926). We sample $\eta_{\rm true}$ from a Gaussian hyperprior as follows:

$$p(\eta_{\rm true}|\boldsymbol{\theta}) = \mathcal{N}(\eta_{\rm true}|\hat{\eta},\ w_\eta), \tag{15}$$

where $\hat{\eta}$ and w_η denote the mean and standard deviation of the hyperprior, respectively. This is found to be a reliable model for the prior distribution of the latent parameters even when the true values are not Gaussian-distributed (Bartlett & Desmond 2023).

We assign Jeffreys priors to σ_v and $\sigma_{\rm TFR}$, such that $\pi(\sigma_v) \propto 1/\sigma_v$ and $\pi(\sigma_{\rm TFR}) \propto 1/\sigma_{\rm TFR}$. For $\boldsymbol{V}_{\rm ext}$, we use a uniform prior in both magnitude and sky direction. We infer $\hat{\eta}$ with a uniform prior and w_η with a Jeffreys prior. Uniform priors are also set for all remaining parameters. We summarize the model parameters in Table 1. We sample the posterior using the Hamiltonian Monte Carlo (HMC)-based No U-Turns Sampler (NUTS; Hoffman & Gelman 2011) as implemented in the `NumPyro` package (Phan, Pradhan & Jankowiak 2019).[3] Burn-in samples are removed, and we ensure a sufficient number of steps such that the Gelman–Rubin statistic differs from unity by $< 10^{-3}$ (Gelman & Rubin 1992).

We compute the model evidence $\mathcal{Z}$, which is defined as the integral of the product of the likelihood and prior over the parameter space.

$$\mathcal{Z} \equiv \int \mathcal{L}(D|\boldsymbol{\theta})\pi(\boldsymbol{\theta})\mathrm{d}\boldsymbol{\theta}, \tag{16}$$

where D are some data and $\boldsymbol{\theta}$ are the model parameters. The ratio of the evidences for two models, known as the Bayes factor $\mathcal{B}$, quantifies the relative support of the data for one model over another, assuming the two models are equally likely a priori.

Since the flow model outlined above includes two latent variables per galaxy (the true magnitude and linewidth), the posterior of the full inference becomes $\approx 14\,000$-dimensional, rendering the evidence integral computationally infeasible. Consequently, whenever we calculate the evidence, we adopt the approximate flow model described in S25. In this approach, the true magnitude and linewidth are fixed to their observed values – effectively assigning them a Dirac-delta prior – while their uncertainties are linearly propagated into the distance modulus error. For a detailed discussion of this approximation, we refer the reader to Appendix B of S25.

We calculate $\mathcal{Z}$ for the lower dimensional posterior using `harmonic`, a tool that leverages normalizing flows and the harmonic estimator to compute the evidence directly from posterior samples (McEwen et al. 2021; Polanska et al. 2024).[4] To ensure that prior-range effects do not affect the evidence comparison, we adopt identical uniform parameter ranges when comparing different void profiles. When comparing the evidence of a void model to that of a model which assumes the velocity field is described solely by a constant dipole, the void model introduces two additional parameters with uniform priors relative to the dipole-only model: $R_{\rm offset}$, with a uniform prior ranging from -50 to 50 Mpc; and $\tilde{r}_{\rm void}$, with a uniform prior ranging between 0.01 and 3. These two parameters reduce the void model evidence by approximately 2.48 in $\log_{10}$ compared to the fiducial void model, in which they are fixed.

4 RESULTS

In this section, we present the results of calibrating the void model parameters using both the bulk flow curve from W23 and the galaxy-by-galaxy flow model applied to the CF4 TFR galaxy sample with the SH0ES Cepheid absolute calibration. For the latter, we compute the Bayesian evidence to compare different void profiles and identify which is most favoured by the data (Section 4.1.4). Additionally, in Section B, we examine the special case where the void size is fixed to its fiducial value, presenting corrected results for the M24 analysis.

4.1 Galaxy-by-galaxy constraint

4.1.1 Inferred void parameters

In Fig. 2, we present the results of jointly inferring all model parameters (summarized in Table 1) for the three void profiles, following the methodology described in Section 3.3. For all profiles, we find that $\boldsymbol{V}_{\rm ext}$ points towards a consistent direction of $(\ell_{\rm ext},\ b_{\rm ext}) \approx (308^\circ,\ -8^\circ)$ in Galactic coordinates. However, its magnitude varies significantly across the profiles, with the best-fitting values of 230,

[3] https://num.pyro.ai/en/latest/

[4] https://github.com/astro-informatics/harmonic

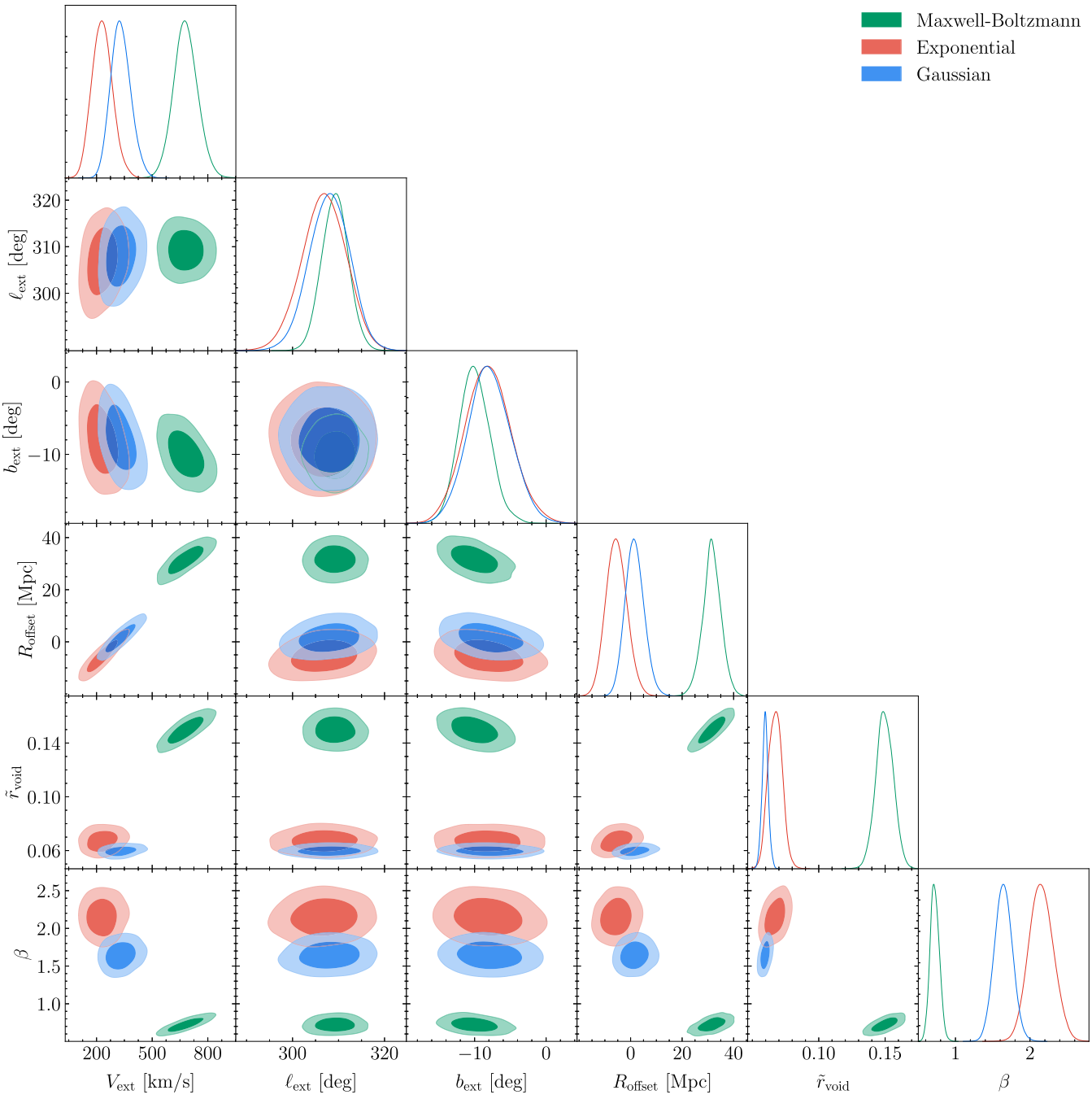

Figure 2. Posterior distributions of the inferred void model parameters obtained by fitting the flow model described in Section 3.3 to the CF4 TFR data. Results are shown for the exponential (red), Gaussian (blue), and Maxwell–Boltzmann (green) void profiles. The sampled parameters include the magnitude and direction of the external velocity $\boldsymbol{V}_{\rm ext}$ in Galactic coordinates, the observer's offset $R_{\rm offset}$ from the void centre along the symmetry axis, the relative void size $\tilde{r}_{\rm void}$, and the velocity scaling parameter β. For all three profiles, we find a preference for significantly smaller void sizes compared to the fiducial sizes in HBK20.

331, and 681 km s^{-1} for the exponential, Gaussian, and Maxwell–Boltzmann cases, respectively, each with a typical uncertainty of ≈ 50 km s^{-1}.

As expected, the magnitude of $\boldsymbol{V}_{\rm ext}$ is degenerate with the observer offset $R_{\rm offset}$, for which we infer values of -5.5 ± 4, 1.5 ± 3.6, and 31.5 ± 3.6 Mpc for the exponential, Gaussian, and Maxwell–Boltzmann profile, respectively. While the exponential and Gaussian profiles favour a position near the void centre, the Maxwell–Boltzmann case requires a significantly offset observer. As we will show in Fig. 3, the large $\boldsymbol{V}_{\rm ext}$ effectively counteracts the larger void-induced outflow at $R_{\rm offset}$, since the outflow vanishes at the void centre and rises roughly linearly at small radii.

The most surprising feature of Fig. 2 is the very low inferred fractional void size $\tilde{r}_{\rm void}$, with values of 0.0670 ± 0.0052, 0.0597 ± 0.0024, and 0.1500 ± 0.0066 for the exponential, Gaussian, and Maxwell–Boltzmann profile, respectively. These correspond to pre-

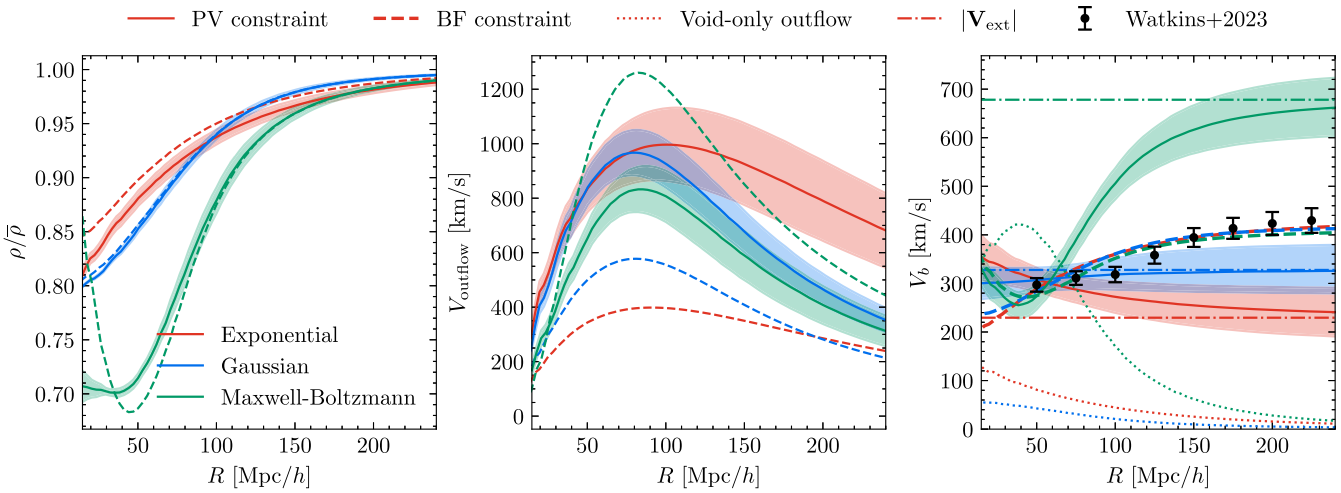

Figure 3. The inferred void density field (left panel), the outflow velocity curve (i.e. the monopole of the velocity field; middle panel), and the bulk flow curve (an integral of the dipole of the velocity field; right panel) as a function of distance from the observer, using the void parameters and their uncertainties as inferred by our field-level analysis. We show results for the exponential (Gaussian; Maxwell–Boltzmann) profile using red (blue; green) shaded bands, which indicate the 1σ uncertainty. In the right panel, the dot–dashed lines show $V_{\rm ext}$ and the dotted lines show the bulk flow without including $\boldsymbol{V}_{\rm ext}$, i.e. that produced intrinsically by the void. The dashed lines show the bulk flow curves in the models that best fit the results of W23, where the colour again indicates the density profile. The W23 results themselves are shown as black points with uncertainties.

ferred initial void sizes of approximately 69, 61, and 34 cMpc, substantially smaller than the fiducial values used in HBK20. Such small voids produce no significant imprint on the CMB quadrupole, making the CMB quadrupole constraint irrelevant.

Lastly, we find that the velocity scaling parameter β is inferred to be 2.15 ± 0.16, 1.64 ± 0.12, and 0.72 ± 0.06 for the exponential, Gaussian, and Maxwell–Boltzmann profiles, respectively. None of the profiles are consistent with $\beta = 1$, indicating that the fiducial void-predicted velocities require rescaling. Specifically, the exponential and Gaussian profiles underestimate the outflow velocities (for the best-fitting small $\tilde{r}_{\rm void}$), while the Maxwell–Boltzmann profile overestimates them. For the exponential and Gaussian profiles, these results suggest a smaller but deeper void than reported in HBK20, an issue we investigate next.

4.1.2 *Inferred void density and velocity profiles*

A much smaller local void implies a more rapid rise in density towards the cosmic mean, as shown in the left panel of Fig. 3. This density profile is calculated from the final positions of the particle trajectories using equations (54) and (55) of HBK20 for the Maxwell–Boltzmann profile, which we generalize appropriately for the other void profiles. The outflow velocity curve is computed as the mean enclosed radial velocity, whereas the bulk flow curve is computed as the mean enclosed 3D velocity. The middle panel of Fig. 3 illustrates that while the void-induced outflow velocity $V_{\rm outflow}$ increases at a rate comparable to the Hubble tension ($cz' - \dot{a}$), it reaches its peak at significantly smaller radii than those used to measure cz' due to the more compact void profiles.

The right panel of Fig. 3 shows the reconstructed bulk flow curves. None of the preferred models match the results of W23. The exponential and Gaussian profiles yield nearly flat bulk flow curves dominated by $V_{\rm ext}$, as expected given that the inferred observer position is very close to the void centre. In contrast, the Maxwell–Boltzmann profile produces a steeply rising bulk flow curve, driven by the relatively large $V_{\rm ext}$, which sets the asymptotic limit. However, the rapid rise with radius overshoots even the steep bulk flow trend reported by W23. We discuss this further in Section 5.1. It is important to bear in mind that these posterior predictive bulk flows are derived through the lens of the void model and do not represent a general Bayesian inference of the bulk flow from the peculiar velocity data. They do however suggest that such an inference would not agree with the W23 result. The void models predict a bulk flow of $\approx 300\,{\rm km\,s^{-1}}$ at the origin, where we also have the constraint that the LG motion with respect to the CMB is $620 \pm 15\ {\rm km\,s^{-1}}$ (Planck Collaboration I 2020a). These are consistent given the velocity dispersion parameter $\sigma_v \approx 350\,{\rm km\,s^{-1}}$, which describes the scatter between the motion of individual tracers (such as a halo hosting the LG) and the smooth large-scale velocity field captured by the void models.

4.1.3 *Predicted local H_0*

Although the velocity data does appear to favour the existence of a void, the fact that it is much smaller than the HBK20 model means that the outflow velocity is too low and peaks too quickly to solve the Hubble tension. Local measurements of cz' typically correspond to distances of 100–600 Mpc ($z = 0.023$–0.15; Camarena & Marra 2020), well beyond the outflow peak. We quantify this by computing the Hubble constant $H_0^{\rm local} \equiv cz'$ that would be inferred locally in these models, following the method described in section 3.3.4 of HBK20. We note that the actual value of H_0, or the present $\dot{a}$, is $67.4\,{\rm km\,s^{-1}\,Mpc^{-1}}$ in all models.

In Fig. 4, we show that the very small inferred void sizes limit the ability of the Gaussian and Maxwell–Boltzmann profiles to fully resolve the Hubble tension. Specifically, they yield $H_0^{\rm local} = 70.40^{+0.43}_{-0.38}$ and $70.18^{+0.48}_{-0.40}\ {\rm km\,s^{-1}\,Mpc^{-1}}$, respectively – about 3σ below the four-anchor SH0ES measurement of $73.17 \pm 0.86\ {\rm km\,s^{-1}\,Mpc^{-1}}$ (Breuval et al. 2024). In contrast, the exponential void profile remains a plausible solution, producing $H_0^{\rm local} = 72.08^{+0.86}_{-0.80}\ {\rm km\,s^{-1}\,Mpc^{-1}}$, which is consistent with local determinations (Uddin et al. 2024). In fact, this $H_0^{\rm local}$ is only 1σ below the SH0ES measurement and only

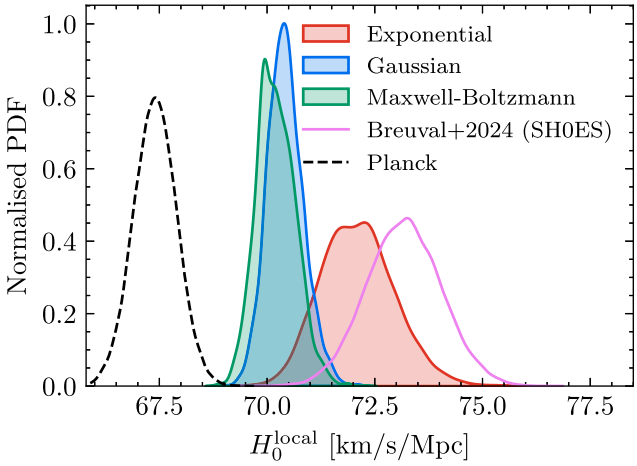

Figure 4. Posterior predictive distributions of $H_0^{\rm local}$ when jointly varying the void size and velocity scaling parameter β for the exponential, Gaussian, and Maxwell–Boltzmann void profiles (shown in red, blue, and green respectively). We find $H_0^{\rm local} = 72.08^{+0.86}_{-0.80}$, $70.40^{+0.43}_{-0.38}$, and $70.18^{+0.48}_{-0.40}$ km s^{-1} Mpc^{-1} for the exponential, Gaussian, and Maxwell–Boltzmann profiles, respectively. For comparison, we show the *Planck* and four-anchor SH0ES H_0 (Planck Collaboration VI 2020b; Breuval et al. 2024) as unfilled dashed black and solid magenta distributions, respectively. The *Planck* H_0 is the background value assumed by the void models.

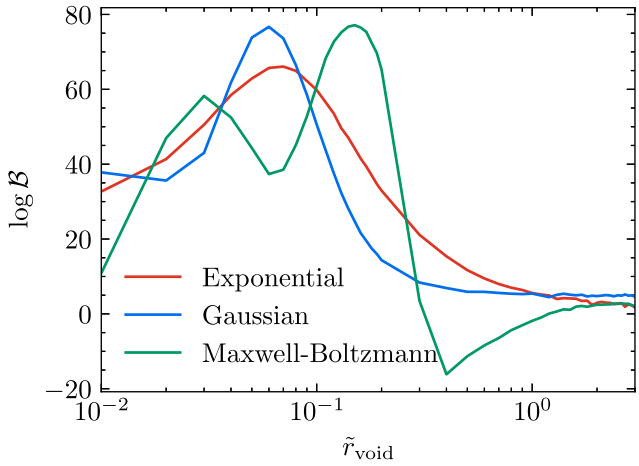

Figure 5. The logarithmic Bayes factor for a grid of void sizes, which we hold fixed during each inference. The Bayes factors are relative to a model where the velocity field is modelled only by a constant dipole $\boldsymbol{V}_{\rm ext}$, with positive values indicating a preference over this simple void-free model. While most of the probed range of void sizes is preferred over the simpler pure dipole model with no net outflow, the preference is much stronger for voids significantly smaller than the fiducial size found by HBK20. The two preferred models are the Gaussian and Maxwell–Boltzmann profiles with $\tilde{r}_{\rm void} \approx 0.06$ and 0.15, respectively.

$1-2\sigma$ below the slightly higher more recent measurements with little or no reliance on SNe Ia (Boubel et al. 2024; Jensen et al. 2025; Scolnic et al. 2025; Vogl et al. 2025). We note that in these studies, the top rung of the distance ladder uses techniques that do not reach out as far as SNe Ia, so $H_0^{\rm local} \equiv cz'$ has to be estimated using a more limited redshift range (e.g. $z = 0.023$–0.1 for Scolnic et al. 2025). Given the small void sizes inferred in our analysis, working out the local cz' over a narrower redshift range would most probably slightly increase the model value, further reducing the tension.

4.1.4 Model selection

We now compare the performance of the void models using a Bayesian evidence analysis (Jeffreys 1939). The resulting $\log \mathcal{B}$ is 10.7 (9.4) for the Gaussian (Maxwell–Boltzmann) profile relative to the result for the exponential profile. The positive values in both cases show that the exponential profile is strongly disfavoured compared to the other profiles. However, the difference between the Gaussian and Maxwell–Boltzmann profiles is modest, indicating only weak preference for the Gaussian model despite the markedly different preferred value of $\boldsymbol{V}_{\rm ext}$. We note that these Bayesian evidences do not take into account measurements of the local cz', which we saw in the previous section clearly prefers the Exponential model (Fig. 4).

To better understand the impact of introducing the velocity scaling parameter β, we also consider models with fixed $\beta = 1$. In this case, we find $\log \mathcal{B} = 17.3$ (22.7) for the Gaussian (Maxwell–Boltzmann) profile relative to the exponential profile result. This implies a strong preference for the Maxwell–Boltzmann model if $\beta = 1$. Notably, however, the evidence for the Maxwell–Boltzmann profile remains nearly unchanged with or without β, while the exponential and Gaussian models gain significantly from allowing β to vary, improving by approximately 13 and 6 in $\log \mathcal{B}$, respectively. This suggests that jointly varying both the relative void size and the velocity scaling parameter (effectively analogous to the initial void underdensity) is essential for a good fit to the distance and redshift data, except in the case of the Maxwell–Boltzmann profile.

To investigate this further, we compute $\mathcal{B}$ for a grid of void sizes, holding $\tilde{r}_{\rm void}$ fixed each time (the 'profile Bayes factor'). The scaled void radius is increased in steps of 0.01 up to $\tilde{r}_{\rm void} = 0.2$, and in steps of 0.1 beyond that. Our results are presented in Fig. 5, where we show the Bayes factors relative to a model in which the velocity field is modelled solely by $\boldsymbol{V}_{\rm ext}$. Despite the higher complexity of the void models, they are strongly preferred by the data over a model with fixed $\boldsymbol{V}_{\rm pec} = \boldsymbol{V}_{\rm ext}$ throughout the considered volume for most considered values of $\tilde{r}_{\rm void}$. For the exponential and Gaussian profiles, this is true even for the fiducial void size found by HBK20. As expected, the exponential, Gaussian, and Maxwell–Boltzmann profiles exhibit maxima near $\tilde{r}_{\rm void} \approx 0.07$, 0.06, and 0.15, respectively. For smaller void sizes, the underdense region becomes negligible, leading to virtually no outflow. Fig. 5 also shows that larger void sizes, particularly the fiducial size proposed by HBK20, are disfavoured by the data compared to smaller voids, which provide a better fit. It will be interesting to explore the extent to which such a small void would be consistent with other data sets, but this goes beyond the scope of this work.

4.1.5 Distance to the Coma Cluster

As a posterior predictive check of the void models, we examine their predictions for the redshift of the Coma Cluster, one of the most massive and extensively studied nearby galaxy clusters (e.g. Peebles 1970; Colless & Dunn 1996; Pimbblet, Penny & Davies 2014). Recently, Scolnic et al. (2025) used a calibration of the SNe Ia absolute magnitude based on the *HST* distance ladder to estimate a distance to Coma of 98.5 ± 2.2 Mpc, along with a CMB-frame observed redshift of 0.02445 ± 0.00024. This is consistent with other recent estimates such as Benisty et al. (2025), who report a heliocentric redshift of 0.02333 ± 0.00013, corresponding to 0.02424 ± 0.00013 in the CMB frame. Scolnic et al. (2025)

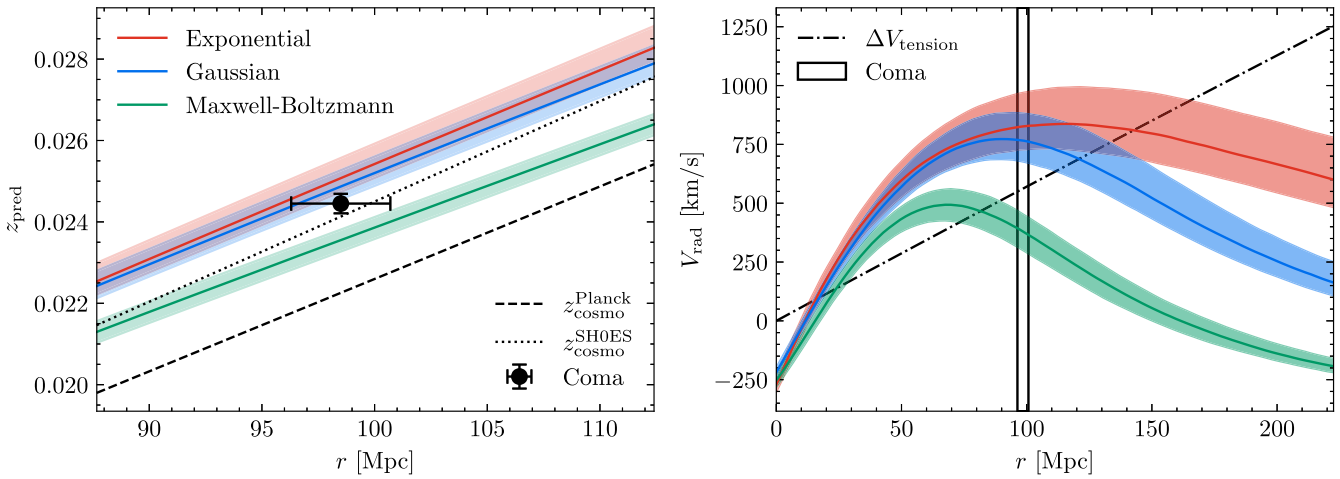

Figure 6. Predicted redshift of the Coma Cluster as a function of its comoving distance r (left panel) and the corresponding radial velocity profile (right panel), shown for the three void profiles. The shaded bands indicate the 1σ uncertainty regions. For the Coma Cluster, we assume $r = 98.5 \pm 2.2$ Mpc and $z_{\rm obs} = 0.02445 \pm 0.00024$ (Scolnic et al. 2025), both shown with 1σ error bars. The dashed and dotted black lines in the left panel show the redshift–distance relation for the *Planck* and SH0ES values of H_0, respectively, assuming no peculiar velocity in either case. In the right panel, the vertical band indicates the 1σ distance to Coma from the *HST* distance ladder calibration, while the dash–dotted line shows the peculiar velocity required in the *Planck* cosmology to reproduce the same total redshift at a given physical distance as in the SH0ES cosmology with no peculiar velocity ($\Delta V_{\rm tension}$). The observed redshift and distance of Coma imply a slightly higher local cz' than in the SH0ES cosmology (Scolnic et al. 2025). Given the observed redshift of Coma, both the exponential and Gaussian profiles yield predictions consistent with its observed distance, which the Maxwell–Boltzmann profile mildly overestimates at the 2σ level.

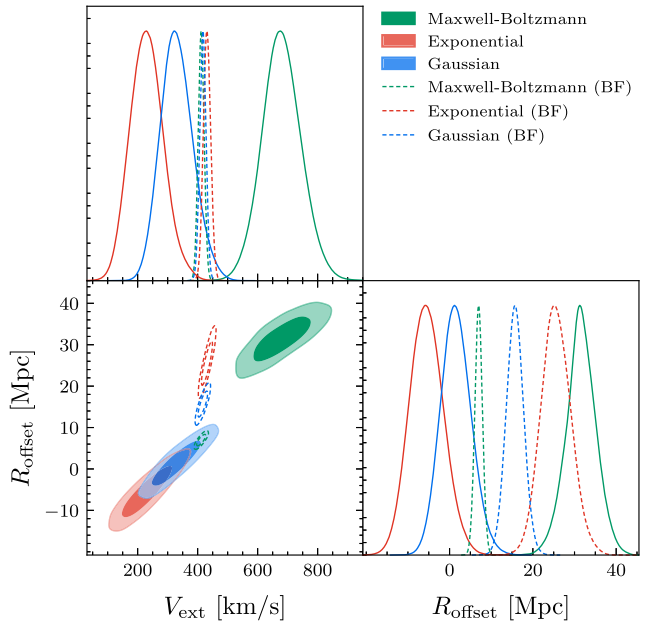

Figure 7. Comparison of the void systemic velocity magnitude $V_{\rm ext}$ and the observer offset $R_{\rm offset}$ between the field-level analysis (based on the CF4 catalogue) and the bulk flow constraints ('BF', measured by W23 but also based on CF4). The discrepancy casts doubt on their bulk flow inference as the underlying data are the same in both cases.

emphasized that this distance is substantially lower than the value inferred from the *Planck* cosmology assuming negligible peculiar velocity. Reconciling the observed redshift with the calibrated distance would require a mean peculiar velocity exceeding 500 km/s, despite no velocity reconstructions predicting an abnormally large peculiar velocity for Coma (e.g. Carrick et al. 2015; Jasche & Lavaux 2019; Lilow & Nusser 2021).

The void models we consider naturally produce such outflows while assuming the *Planck* H_0 at the background level. The left panel of Fig. 6 shows the predicted redshift $z_{\rm pred}$ as a function of comoving distance r to Coma, while the right panel shows the corresponding radial velocity profile. Among the models, the Gaussian profile shows the best agreement with the calibrated Coma distance, though the exponential profile yields a prediction that is only marginally different. In contrast, the Maxwell–Boltzmann profile, due to its weaker outflow, overpredicts the distance to Coma at the 2σ level.

4.2 Bulk flow constraints

We now perform a χ^2 analysis by fitting the void model to the bulk flow curve of W23 (Section 3.2). This will allow us to correct the factor of 3 error described in Section 3.2, while updating the constraints according to our field-level findings. For computational efficiency, we fix the relative void sizes to the best-fitting values from the previous section: 7, 6, and 15 per cent for the exponential, Gaussian, and Maxwell–Boltzmann profile, respectively. We sample the observer offset $R_{\rm offset}$ and external velocity $\boldsymbol{V}_{\rm ext}$, assuming its direction is aligned with the previously inferred best-fitting direction from the galaxy-by-galaxy analysis. The goal is to assess whether these more compact void profiles still allow for a satisfactory fit to the observed bulk flow.

In Fig. 7, we compare the results of this fit to those from the galaxy-by-galaxy flow model. We find that even such relatively small voids can reproduce the W23 bulk flow curve well. For the exponential profile, the best fit is obtained at $R_{\rm offset} = 25$ Mpc and $V_{\rm ext} = 430$ km s^{-1}, with a minimum $\chi^2 = 9.14$. The Gaussian profile yields a best fit at $R_{\rm offset} = 16$ Mpc and $V_{\rm ext} = 419$ km s^{-1}, with $\chi^2 = 9.40$. Lastly, the Maxwell–Boltzmann profile yields a best fit at $R_{\rm offset} = 7$ Mpc and $V_{\rm ext} = 412$ km s^{-1}, with $\chi^2 = 11.01$. All these χ^2 values are very reasonable for nine data points and two free parameters.

However, these best-fitting parameters are in significant tension with those inferred from the flow model analysis, which favours

substantially lower values of both $V_{\rm ext}$ and $R_{\rm offset}$. This discrepancy is a manifestation of the fact that the flow model prefers nearly flat or even declining bulk flow curves for the exponential and Gaussian profiles (Fig. 3), while fitting directly to the bulk flow curve forces the model to produce an increasing trend with radius, pushing the fit toward higher $V_{\rm ext}$ and larger offsets. The other unexpected feature is that the uncertainties appear smaller in the bulk flow fit. This may suggest that the error bars reported by W23 are underestimated (as noted by Whitford et al. 2023), or it could reflect the simplifying assumption in these constraints that the bulk flow measurements are statistically independent.

Lastly, to connect with the analysis of M24, we present updated results using the corrected definition while keeping the void size fixed to its fiducial value (Section B1). We find that the fiducial size void profiles remain capable of reproducing the bulk flow curve measured by W23, although they now favour different values of $\boldsymbol{V}_{\rm ext}$ and $R_{\rm offset}$ compared to the original analysis. This suggests that the W23 bulk flow curve can be reproduced with little difficulty by the considered void models, which is not the case in ΛCDM (see their fig. 8).

5 DISCUSSION

5.1 Implications and significance of the results

For the first time, we test the local void scenario for the Hubble tension (HBK20) and constrain its degrees of freedom by comparing with direct distances to individual galaxies, which combined with their redshifts tells us their peculiar velocity. In particular, we evaluate the void models directly against the relevant galaxy observables (sky position, redshift, linewidth, and apparent magnitude) using the field-level flow model described in Section 3.3, while jointly inferring the parameters of the TFR used to estimate redshift-independent distances from the linewidth (equation 2). Our models assume a background *Planck* cosmology that fits the CMB anisotropies (Planck Collaboration VI 2020b; Tristram et al. 2024; Calabrese et al. 2025; Camphuis et al. 2025).

For the fiducial void size, our field-level inference of $\boldsymbol{V}_{\rm ext}$ and $R_{\rm offset}$ yields results consistent at $< 2\sigma$ with those obtained from fitting to the W23 bulk flow curve under the assumption of independent data points (Fig. B3). Moreover, we find excellent agreement between the bulk flow direction inferred from the CF4 data set and that reported by W23. However, we find significantly different results when we relax the assumption of a fixed void size and allow for an effect similar to variation in the initial void depth, captured through a velocity scaling parameter β. In these extended models, our field-level analysis implies bulk flow curves dominated by the external velocity $\boldsymbol{V}_{\rm ext}$. With the exception of the poorly-fitting Maxwell–Boltzmann void profile, the posterior predicted bulk flow curves do not rise, in disagreement with the result of W23. This is potentially related to the findings of Whitford et al. (2023) that the uncertainties in the bulk flow estimator are likely larger than those quoted by W23, particularly the latter's claim of achieving 37 km s^{-1} precision out to 200 Mpc h^{-1}.

The void scenario was previously tested by M24 using the bulk flow curve from W23. However, their analysis contained a significant flaw in the definition of the bulk flow (see Section 3.2). Adopting the correct formulation and generalizing the HBK20 model to include an arbitrary systemic void velocity $\boldsymbol{V}_{\rm ext}$ in addition to the void outflow, we find that a good fit to the W23 bulk flow curve is possible, provided the observer lies within $\lesssim 50$ Mpc of the void centre (as discussed in Section B). However, this agreement no longer constitutes an a priori prediction of the void model. Rather, it highlights that the generalization of the void model's systemic velocity allows for the reproduction of a broad range of bulk flow curves, including that of W23. This is because the void scenario generically assumes enhanced growth of structure compared to ΛCDM on $\gtrsim 100$ Mpc scales, which aligns well with the implications of the W23 result.

Crucially, our main analysis shows that the CF4 peculiar velocity data prefers significantly smaller void sizes for all profiles compared to the fiducial void size found by HBK20. While our approach tests the predicted velocity field on a galaxy-by-galaxy basis, HBK20 constrain the void using source number densities and its ability to resolve the Hubble tension. The two methods are complementary but distinct, and their discrepancy may point either to limitations of the KBC void model itself – such as some systematic bias – or to the need for a more complex void density profile. It is interesting to note that when calibrating the void model to match the bulk flow curve of W23, the χ^2 comparison favours the fiducial void size over the smaller sizes preferred by the field-level analysis (Section B1).

While the bulk flow is a useful summary statistic, there are uncertainties when estimating it from the CF4 survey (Tully et al. 2023). CF4 combines several dedicated surveys with varying sky coverage, which implies that any magnitude mis-calibration could introduce spurious bulk flows that increase with distance. This is due to the gradient of redshift with respect to distance modulus, $\mathrm{d}(cz_{\rm cosmo})/\mathrm{d}\mu$. Consequently, a zero-point calibration offset as small as 0.017 mag – corresponding to the statistical 1σ uncertainty in the calibration of the TFR or fundamental plane zero-point relative to SNe Ia in the CF4 catalogue (see fig. 16 of Tully et al. 2023) – would induce an artificial flow of 76 (152) km s^{-1} at 100 (200) Mpc h^{-1}. This concern is particularly relevant for CF4, where the sources beyond 150 Mpc h^{-1} come almost exclusively from the SDSS fundamental plane dataset. Another potential concern is that the methodology of W23 underestimates uncertainties by a factor of ≈ 3.5, with this discrepancy increasing at larger distances, precisely where W23 reports the strongest tension with ΛCDM (Whitford et al. 2023).

Using a Bayesian evidence comparison, as presented in Fig. 5, we find that the Gaussian profile is marginally preferred over the Maxwell–Boltzmann profile, while the exponential profile is decisively disfavoured. This outcome is somewhat surprising given that the Gaussian and Maxwell–Boltzmann profiles favour significantly different values of $\boldsymbol{V}_{\rm ext}$. In the Maxwell–Boltzmann case, the predicted bulk flow magnitude approaches ≈ 700 km s^{-1} at $R > 200$ Mpc h^{-1} because $\boldsymbol{V}_b \to \boldsymbol{V}_{\rm ext}$ at large radii due to the decay of the void-induced outflow. However, taking this extrapolation at face value is problematic, as the majority of the data lies at much smaller radii: the CF4 galaxy distribution peaks near 60 Mpc h^{-1} and drops off sharply beyond 120 Mpc h^{-1} (Fig. 1). At the peak, the large $\boldsymbol{V}_{\rm ext}$ acts to cancel the void-induced outflow due to the significantly offset observer position, which may dominate the likelihood. This comes at the cost of overpredicting the bulk flow for the relatively few galaxies located beyond 100 Mpc h^{-1}, since the assumption of a constant external flow is clearly too simplistic. Despite these difficulties, the exponential and Gaussian void models are preferred over a simpler $\boldsymbol{V}_{\rm ext}$-only model with no void outflow and thus effectively no void, for all void sizes (see Fig. 5).

Although a small void can reproduce the W23 bulk flow curve if calibrated to it (see the right panel of Fig. 3), the preferred parameters are discrepant with those based on the field-level analysis of either profile. Furthermore, out of the smaller void models preferred by our field-level analysis, only the exponential profile produces a sufficiently large outflow to match the observed $H_0^{\rm local} \equiv cz'$ at just

over 1σ. However, it is also the least favoured profile according to our field level analysis with free void size. This instead favours the Gaussian and Maxwell–Boltzmann profiles, which however still leave a residual 3σ Hubble tension as they are only able to account for about half of it. This limitation arises because the outflow velocity peaks at low radii, leading to only a modest increase in cz' over the redshift range commonly used to infer it ($z = 0.023 - 0.15$, e.g. Riess et al. 2022). The Hubble tension can be fully resolved with the fiducial void sizes considered by HBK20, which however are larger than the preferred sizes inferred here. None the less, these results demonstrate that (for the data we use) a local void remains a viable mechanism for alleviating the Hubble tension, even if not fully resolving it. Note that our field-level analysis could conceivably have inferred $\beta < 0$ and placed us in an overdensity, since only velocity data are used in the fit. Moreover, the Bayesian evidence could have favoured the simpler $\boldsymbol{V}_{\rm ext}$-only model.

It is interesting to consider why our field-level analysis consistently favours such a small void size when this parameter is allowed to vary, especially if one accepts the presence of a large-scale underdensity in the luminosity density extending out to 300 Mpc, as posited in the KBC void scenario upon which the fiducial void sizes were originally based (Keenan et al. 2013). One possibility is that this could hint at a generally more complex void profile, e.g. a 'void-in-void' configuration, whereby the KBC void encompasses a smaller void that contains the LG. A more complex structure, which necessitates the inclusion of an accurate description of smaller scales, implies a departure from just a spherically symmetric smooth large-scale void, as is described by the HBK20 models. The void-in-void scenario is disfavoured by our analysis given the absence of any secondary features in $\log \mathcal{B}$ at void sizes comparable to that inferred by HBK20 (see Fig. 5), at least for the exponential and Gaussian profiles, which we consider more promising on other grounds (see Fig. 3). Importantly, given that the CF4 catalogue extends robustly only to ≈ 120 Mpc (Fig. 1) and becomes increasingly sparse beyond that, the outer regions of any larger scale underdensity are only weakly probed. Thus, the velocity imprint of a more extended, shallower component of the void could plausibly evade detection in the present analysis. A more sophisticated treatment would likely be required to capture the full dynamics of such a configuration.

Another possibility is simply that the Hubble tension should be solved with a smaller and most likely deeper void than inferred by HBK20. We note that part of the reason HBK20 preferred such large void sizes is to fit the high H_0 values from H0LiCOW strong lensing time delays (Wong et al. 2020). Subsequent updates to this analysis indicate good agreement with $H_0^{\rm Planck}$ (Birrer et al. 2020; Li et al. 2025), as is also the case with strong lensing time delays of SN Refsdal (Kelly et al. 2023; Grillo et al. 2024) and CC results at similar redshifts (Cogato et al. 2024; Guo et al. 2025). This calls for a more rapid decay to the effects induced by a local void. Since we have already seen that an exponential void with a much smaller size than inferred by HBK20 can adequately explain the locally measured cz' (Fig. 4) and the CF4 galaxy data at the field level, it is worthwhile to explore if it can fit other observations and yield redshifts at fixed distance that converge at the correct rate to those in the background *Planck* cosmology (Mazurenko et al. 2025). We note that since the galaxy number counts of Keenan et al. (2013) are in redshift rather than real space and the effect of a void on redshifts would persist even after the density has returned to the cosmic mean, it is conceivable that their reported luminosity underdensity can be recovered by the smaller voids proposed here (especially if the void is deeper than considered by HBK20).

As described in Section 2, we use an absolute calibration of the CF4 TFR using 12 galaxies with Cepheid distances measured as part of the SH0ES project. This partially breaks the degeneracy between H_0 and the normalization of the TFR, making our analysis somewhat sensitive to H_0 directly. We find that the absolute calibration has virtually no effect on the inferred void size, with the preferred value shifting by $\lesssim 1$ per cent. Likewise, neither $V_{\rm ext}$ nor $R_{\rm offset}$ change appreciably for the exponential or Gaussian profiles. Only in the case of the Maxwell–Boltzmann profile does $V_{\rm ext}$ increase, reaching $\approx 900\,{\rm km\,s^{-1}}$ when no absolute calibration is applied and $\beta = 1$.

In contrast, the inclusion of the absolute calibration significantly impacts β: without it, β remains unconstrained due to degeneracies with the void outflow and the TFR normalization. These degeneracies are only broken when an absolute calibration is imposed. In our analysis, the local Hubble constant depends on the void size and the velocity scaling parameter β as

$$H_0^{\rm local}(\beta) = H_0^{\rm Planck} + \beta \left(H_0^{\rm local}\big|_{\beta=1} - H_0^{\rm Planck} \right), \tag{17}$$

as β scales the deviations from the background *Planck* cosmology and the void size enters only through $H_0^{\rm local}\big|_{\beta=1}$, the predicted $H_0^{\rm local}$ when $\beta = 1$. Since the inferred void size is unaffected by the absolute calibration, in practice the calibration affects $H_0^{\rm local}$ only through β. If β were fixed to unity and no absolute calibration applied, the resulting $H_0^{\rm local}$ would be approximately $69.25^{+0.32}_{-0.26}$, $68.89^{+0.21}_{-0.19}$, and $72.31^{+0.27}_{-0.24}\,{\rm km\,s^{-1}\,Mpc^{-1}}$ for the exponential, Gaussian, and Maxwell–Boltzmann profiles, respectively. Under these conditions, the exponential void would no longer provide a viable resolution to the Hubble tension, while the Maxwell–Boltzmann profile would predict an $H_0^{\rm local}$ consistent with SH0ES. However, including absolute calibration favours $\beta < 1$ for the Maxwell–Boltzmann void, which shifts its predicted $H_0^{\rm local}$ closer to the *Planck* value.

5.2 Caveats and future work

A potential limitation of our approach is the assumption that the void and associated outflow velocities arise within a gravity model featuring faster structure growth than predicted by ΛCDM (hence faster outflow velocity for given final density). To circumvent the fact that a void with the size and depth of the KBC void cannot arise in ΛCDM, HBK20 adopted a MOND-based framework. Other gravity models giving faster-than-ΛCDM structure growth (e.g. theories with new gravitational degrees of freedom or fifth forces) will produce somewhat different outflows for a given density profile. As an alternative strategy, one could adopt a fully ΛCDM-based void and constrain the rarity of the initial underdensity preferred by the peculiar velocity data, while still assuming the present $\dot{a} = H_0^{\rm Planck}$ at the background level. It is possible that since our analysis implies a much smaller void than reported by Keenan et al. (2013), such a small void is actually consistent with ΛCDM, though the measured $H_0^{\rm local}$ is not.

We note four further caveats. First, we did not vary the initial void depth directly; instead, we introduced a less physical proxy parameter β to rescale the predicted velocities and approximate the effects of varying the initial underdensity. This was to remove the computational cost of having to calculate the velocity field in a very large number of models. Secondly, we assumed that the observer lies along the void's axis of symmetry, a simplification necessitated by the practical constraints of the void model. Third, our inference of the void properties is dependent on the adopted background value of H_0. Our choice here, $\dot{a} = H_0^{\rm Planck}$, was motivated by the possibility of solving the Hubble tension entirely through void

outflows. Adopting instead $\dot{a} \approx 75\ \mathrm{km\,s^{-1}\,Mpc^{-1}}$ would eliminate most if not all the evidence for a local underdensity, as the peculiar velocities would become much smaller. However, it is unclear how such a high present $\dot{a}$ can arise given the CMB power spectrum and the indications from BAO measurements of a faster expansion rate than the *Planck* cosmology at $z \approx 0.5$–1 (Hamidreza Mirpoorian et al. 2025; Mukherjee & Sen 2025; DESI Collaboration 2025a, b). Preserving the angular diameter distance to recombination requires a compensatory period with sub-*Planck* expansion rate at $z \lesssim 0.5$. Inferring the local density with less sensitivity to H_0 must utilize alternative information such as galaxy number densities (e.g. Jasche & Wandelt 2013; Lavaux & Jasche 2016; Jasche & Lavaux 2019). Fourth, the velocity structure of any local void will be more complex than the simplified spherically symmetric outflow plus systemic motion model explored here, which may be significant for our field-level results.

Future possibilities also lie in expanding the data used. In this work, we used the CF4 TFR galaxies, 12 of which have absolute distance calibrations from the SH0ES Cepheid calibration (Riess et al. 2022) after application of our quality cuts. While the TFR sample offers full sky coverage, its primary limitation is its shallow depth, with only a small fraction of galaxies at redshifts $z_{\mathrm{obs}} > 0.05$. Nevertheless, the TFR remains attractive because it can be recalibrated straightforwardly, without requiring a full covariance matrix – as is necessary for data sets like Pantheon+. In contrast, fundamental plane or SNe samples probe to significantly higher redshifts, potentially offering complementary constraints.

If a void were to extend to scales much larger than those currently probed, this would likely result in an unacceptably large bulk flow – unless the observer were located near the void centre, which becomes increasingly improbable for larger voids. It is statistically implausible for us to reside at the exact centre of a large void: the geometric volume corresponding to such a position is vanishingly small, but observers are expected to be randomly distributed within the cosmic web. For an observer uniformly distributed in volume, the probability density of lying at distance R_{offset} from the void centre is $p(R_{\mathrm{offset}}) = 3R^2_{\mathrm{offset}}/R^3_{\mathrm{void}}$, where R_{void} is the void radius. Thus, for a fixed R_{offset}, the probability falls off as R^{-3}_{void}, making the same offset increasingly unlikely in larger voids. Moreover, the dynamics of voids do not single out the centre as a preferential location for haloes, since galaxies inside voids typically experience outflows away from the centre. Thus, although we may lie close to the centre of a void, the hypothesis that we occupy its precise centre is highly unlikely. Even in that case, exponential or Gaussian voids with $\tilde{r}_{\mathrm{void}} > 0.5$ would predict $H_0^{\mathrm{local}} \approx 77\ \mathrm{km\,s^{-1}\,Mpc^{-1}}$, substantially exceeding the SH0ES value of $73.17 \pm 0.86\ \mathrm{km\,s^{-1}\,Mpc^{-1}}$ and therefore overresolving the Hubble tension. This problem could be alleviated by scaling down the outflow velocities using $\beta < 1$.

6 CONCLUSIONS

We have investigated the local void model of HBK20 for addressing the Hubble tension, which was motivated by the KBC void (Keenan et al. 2013), a reported underdensity in near-infrared galaxy number counts corresponding to an ≈ 20 per cent matter underdensity extending out to 300 Mpc in radius. While the original analysis by HBK20 did not consider constraints from local peculiar velocity data beyond the LG, we introduce and implement this key observational test. Prior to our work, M24 calibrated the void model using the measured bulk flow curve of W23, but their analysis was limited by reliance solely on these measurements and impacted by an important error, which requires the predictions of M24 to be tripled. To address this, we employed the galaxy-by-galaxy flow model of S25, forward-modelling the observed redshift, apparent magnitude, and linewidth of each TFR galaxy under the assumption of a predicted peculiar velocity field from the void model. By requiring consistency with the observed redshifts in the CF4 catalogue, we derived corresponding constraints on the preferred void parameters: its size, systemic velocity relative to the CMB frame, observer offset, and a velocity scaling parameter β that effectively captures variations in the initial void depth. Since β can be < 0, our analysis allows the local density to exceed the cosmic average.

Our main conclusions are as follows:

(i) The CF4 TFR peculiar velocity data favour void sizes that are 7, 6, and 15 per cent of the fiducial size in HBK20, corresponding to 69, 61, and 34 cMpc for the exponential, Gaussian, and Maxwell–Boltzmann profiles, respectively.

(ii) Although the void model is flexible enough to reproduce the measured bulk flow curve of W23, the field-level analysis favours either a flat bulk flow curve for the exponential and Gaussian profiles, or a steeply rising one for the Maxwell–Boltzmann profile. This casts doubt on the bulk flow inference of W23, which should be simply a summary statistic of the galaxy-by-galaxy distance data and hence produce constraints that are consistent with it. All cases are dominated by a constant external velocity $\boldsymbol{V}_{\mathrm{ext}}$, so we advise caution in interpreting the Maxwell–Boltzmann bulk flow due to limited data at large distances.

(iii) The Gaussian and Maxwell–Boltzmann voids yield $H_0^{\mathrm{local}} \approx 70.4 \pm 0.4\ \mathrm{km\,s^{-1}\,Mpc^{-1}}$, which remains 3σ below the local measurement of $73.2 \pm 0.9\ \mathrm{km\,s^{-1}\,Mpc^{-1}}$ (Breuval et al. 2024). In contrast, the larger outflow in the exponential profile provides $H_0^{\mathrm{local}} \approx 72.1 \pm 0.8\ \mathrm{km\,s^{-1}\,Mpc^{-1}}$, within 1σ of Breuval et al. (2024).

(iv) Without considering any expansion rate or source number count data, Bayesian model selection using the observed velocity field favours the Gaussian and Maxwell–Boltzmann profiles over the exponential profile. The Gaussian profile is only marginally preferred over the Maxwell–Boltzmann profile, despite their drastically different kinematic signatures. The fiducial size void profiles, while disfavoured compared to the smaller void sizes preferred by our analysis, are none the less still preferred over a simpler model with constant $\boldsymbol{V}_{\mathrm{ext}}$ (essentially a void-free control model) in the exponential and Gaussian cases, and only mildly disfavoured in the Maxwell–Boltzmann case.

(v) Given the redshift of the Coma Cluster, the exponential and Gaussian profiles are consistent with its measured distance under the *HST* distance ladder calibration (underpredicting it at $< 1\sigma$), while the Maxwell–Boltzmann profile overpredicts it at the 2σ level.

In summary, we find that allowing the relative void size, external velocity, and velocity scaling to vary yields a better fit across all profiles compared to the best-fitting model of HBK20. This suggests that, although their original model may in principle resolve the Hubble tension, the CF4 TFR data instead favour smaller and possibly deeper void profiles, which for the exponential profile only can still solve the Hubble tension at just over 1σ. For the void to remain as a potentially valid solution to the Hubble tension, it will be important to investigate both the extent to which a smaller void than considered in HBK20 can fit other constraints and the extent to which void models with more complex density profiles can simultaneously fit all observables. This is especially important given that the H0LiCOW analysis suggesting the Hubble tension persists out to quite high redshift is no longer considered valid (Birrer et al.

2020), with more modern studies suggesting a more rapid decay to the *Planck* distance–redshift relation (Jia et al. 2023; Jia et al. 2025). Lastly, it will also be interesting to develop theoretical frameworks that could create the proposed enhancement to structure on $\gtrsim 100$ Mpc scales relative to ΛCDM while preserving its success with the CMB anisotropies.

ACKNOWLEDGEMENTS

RS acknowledges financial support from STFC Grant no. ST/X508664/1, the Snell Exhibition of Balliol College, Oxford, and the Center for Computational Astrophysics (CCA) Pre-doctoral Program. HD and IB are supported by a Royal Society University Research Fellowship (grant no. 211046). This project has received funding from the European Research Council (ERC) under the European Union's Horizon 2020 research and innovation programme (grant agreement no. 693024).

We thank Pedro Ferreira, Sebastian von Hausegger, Mike Hudson, Pavel Kroupa, Guilhem Lavaux, Sergij Mazurenko, José Antonio Nájera, and Tariq Yasin for useful inputs and discussions. We also thank Jonathan Patterson for smoothly running the Glamdring Cluster hosted by the University of Oxford, where the data processing was performed.

DATA AVAILABILITY

The CF4 data are publicly available.[5] The flow model code and all other data will be made available on reasonable request to the corresponding author.

REFERENCES

Alnes H., Amarzguioui M., 2006, Phys. Rev. D, 74, 103520
Banik I., Kalaitzidis V., 2025, MNRAS, 540, 545
Banik I., Samaras N., 2025, preprint (arXiv:2410.00804)
Banik I., Zhao H., 2022, Symmetry, 14, 1331
Bartlett D. J., Desmond H., 2023, Open J. Astrophys., 6, 42
Benisty D., Wagner J., Haridasu S., Salucci P., 2025, preprint (arXiv:2504.04135)
Bhardwaj A., Matsunaga N., Huang C. D., Riess A. G., Rejkuba M., 2025, ApJ, 990, 63
Birrer S. et al., 2020, A&A, 643, A165
Boubel P., Colless M., Said K., Staveley-Smith L., 2024, MNRAS, 531, 84
Breuval L. et al., 2024, ApJ, 973, 30
Brout D. et al., 2022, ApJ, 938, 110
Cai T., Ding Q., Wang Y., 2025, Phys. Rev. D, 111, 103502
Calabrese E. et al., 2025, preprint (arXiv:2503.14454)
Camarena D., Marra V., 2018, Phys. Rev. D, 98, 023537
Camarena D., Marra V., 2020, Phys. Rev. Res., 2, 013028
Camarena D., Marra V., Sakr Z., Clarkson C., 2022, Class. Quantum Gravity, 39, 184001
Camphuis E. et al., 2025, preprint (arXiv:2506.20707)
Carrick J., Turnbull S. J., Lavaux G., Hudson M. J., 2015, MNRAS, 450, 317
Castello S., Högås M., Mörtsell E., 2022, J. Cosmol. Astropart. Phys., 2022, 003
Cimatti A., Moresco M., 2023, ApJ, 953, 149
Cogato F., Moresco M., Amati L., Cimatti A., 2024, MNRAS, 527, 4874
Colless M., Dunn A. M., 1996, ApJ, 458, 435
Curtis O., McDonough B., Brainerd T. G., 2025, ApJ, 985, 244
DESI Collaboration, 2025a, J. Cosmol. Astropart. Phys., 2025, 021
DESI Collaboration,, 2025b, preprint (arXiv:2503.14738)
Davis T. M., Hinton S. R., Howlett C., Calcino J., 2019, MNRAS, 490, 2948
Di Valentino E., Melchiorri A., Silk J., 2021, ApJ, 908, L9
Di Valentino E. et al., 2025, PDU, 49, 101965
Ding Q., Nakama T., Wang Y., 2020, Sci. China Phys., Mech. Astron., 63, 290403
Famaey B., McGaugh S. S., 2012, Living Rev. Relativ., 15, 10
Feix M., Branchini E., Nusser A., 2017, MNRAS, 468, 1420
Feldman H. A., Watkins R., Hudson M. J., 2010, MNRAS, 407, 2328
Ge F. et al., 2025, Phys. Rev. D, 111, 083534
Gelman A., Rubin D. B., 1992, Stat. Sci., 7, 457
Grillo C., Pagano L., Rosati P., Suyu S. H., 2024, A&A, 684, L23
Guo W. et al., 2025, ApJ, 978, L33
Hamidreza Mirpoorian S., Jedamzik K., Pogosian L., 2025, preprint (arXiv:2504.15274)
Haslbauer M., Banik I., Kroupa P., 2020, MNRAS, 499, 2845
Hellwing W. A., Bilicki M., Libeskind N. I., 2018, Phys. Rev. D, 97, 103519
Hoffman M. D., Gelman A., 2011, preprint (arXiv:1111.4246)
Hoffman Y., Courtois H. M., Tully R. B., 2015, MNRAS, 449, 4494
Hogg D. W., 1999, preprint (arXiv:astro-ph/9905116)
Hubble E. P., 1926, ApJ, 64, 321
Jasche J., Lavaux G., 2019, A&A, 625, A64
Jasche J., Wandelt B. D., 2013, MNRAS, 432, 894
Jeffreys H., 1939, Theory of Probability, Oxford Univ. Press, Oxford
Jensen J. B., Blakeslee J. P., Cantiello M., Cowles M., Anand G. S., Tully R. B., Kourkchi E., Raimondo G., 2025, ApJ, 987, 87
Jia X. D., Hu J. P., Wang F. Y., 2023, A&A, 674, A45
Jia X. D., Hu J. P., Yi S. X., Wang F. Y., 2025, ApJ, 979, L34
Karachentsev I. D., Telikova K. N., 2018, Astron. Nachr., 339, 615
Keenan R. C., Barger A. J., Cowie L. L., 2013, ApJ, 775, 62
Keenan R. C., Barger A. J., Cowie L. L., 2016, Proc. IAU, 11, 295
Kelly P. L. et al., 2023, Science, 380, abh1322
Kenworthy W. D., Scolnic D., Riess A., 2019, ApJ, 875, 145
Kourkchi E., Tully R. B., Anand G. S., Courtois H. M., Dupuy A., Neill J. D., Rizzi L., Seibert M., 2020a, ApJ, 896, 3
Kourkchi E. et al., 2020b, ApJ, 902, 145
Lane Z. G., Seifert A., Ridden-Harper R., Wiltshire D. L., 2025, MNRAS, 536, 1752
Lavaux G., Jasche J., 2016, MNRAS, 455, 3169
Leavitt H. S., Pickering E. C., 1912, Harv. Coll. Obs. Circ., 173, 1
Li T., Collett T. E., Marshall P. J., Erickson S., Enzi W., Oldham L., Ballard D., 2025, MNRAS, 538, 2375
Lilow R., Nusser A., 2021, MNRAS, 507, 1557
Mazurenko S., Banik I., Kroupa P., Haslbauer M., 2024, MNRAS, 527, 4388
Mazurenko S., Banik I., Kroupa P., 2025, MNRAS, 536, 3232
McEwen J. D., Wallis C. G. R., Price M. A., Spurio Mancini A., 2021, preprint (arXiv:2111.12720)
Milgrom M., 1983, ApJ, 270, 365
Moresco M., 2024, preprint (arXiv:2412.01994)
Mukherjee P., Sen A. A., 2025, preprint (arXiv:2503.02880)
Nadathur S., Hotchkiss S., Diego J. M., Iliev I. T., Gottlöber S., Watson W. A., Yepes G., 2015, MNRAS, 449, 3997
Nájera J. A., Desmond H., 2025, MNRAS, 541, 671
Nistane V., Cusin G., Kunz M., 2019, J. Cosmol. Astropart. Phys., 2019, 038
Nusser A., 2016, MNRAS, 455, 178
Nusser A., Davis M., 2011, ApJ, 736, 93
Peebles P. J. E., 1970, AJ, 75, 13
Peery S., Watkins R., Feldman H. A., 2018, MNRAS, 481, 1368
Pesce D. W. et al., 2020, ApJ, 891, L1
Phan D., Pradhan N., Jankowiak M., 2019, preprint (arXiv:1912.11554)
Phillips M. M., 1993, ApJ, 413, L105
Pimbblet K. A., Penny S. J., Davies R. L., 2014, MNRAS, 438, 3049
Planck Collaboration I, 2020a, A&A, 641, A1
Planck Collaboration VI,, 2020b, A&A, 641, A6
Polanska A., Price M. A., Piras D., Spurio Mancini A., McEwen J. D., 2024, preprint (arXiv:2405.05969)
Riess A. G., Casertano S., Yuan W., Bowers J. B., Macri L., Zinn J. C., Scolnic D., 2021, ApJ, 908, L6
Riess A. G. et al., 2022, ApJ, 934, L7
San Martín M., Rubio C., 2023, Ann. Phys., 458, 169444

[5] https://edd.ifa.hawaii.edu/dfirst.php

Scolnic D., Vincenzi M., 2023, preprint (arXiv:2311.16830)
Scolnic D. et al., 2025, ApJ, 979, L9
Scrimgeour M. I. et al., 2016, MNRAS, 455, 386
Seifert A., Lane Z. G., Galoppo M., Ridden-Harper R., Wiltshire D. L., 2025, MNRAS, 537, L55
Shanks T., Hogarth L. M., Metcalfe N., 2019a, MNRAS, 484, L64
Shanks T., Hogarth L. M., Metcalfe N., Whitbourn J., 2019b, MNRAS, 490, 4715
Stiskalek R., Desmond H., Devriendt J., Slyz A., Lavaux G., Hudson M. J., Bartlett D. J., Courtois H. M., 2025, preprint (arXiv:2502.00121)
The Planck Collaboration,, 2006, preprint (arXiv:astro-ph/0604069)
Tripp R., 1998, A&A, 331, 815
Tristram M. et al., 2024, A&A, 682, A37
Tully R. B., Fisher J. R., 1977, A&A, 54, 661
Tully R. B. et al., 2023, ApJ, 944, 94
Uddin S. A. et al., 2024, ApJ, 970, 72
Valcin D., Jimenez R., Seljak U., Verde L., 2025, preprint (arXiv:2503.19481)
Vogl C. et al., 2025, A&A, in press
Watkins R., Feldman H. A., 2015, MNRAS, 447, 132
Watkins R., Feldman H. A., Hudson M. J., 2009, MNRAS, 392, 743
Watkins R. et al., 2023, MNRAS, 524, 1885
Whitford A. M., Howlett C., Davis T. M., 2023, MNRAS, 526, 3051
Wong K. C. et al., 2020, MNRAS, 498, 1420
Wu H.-Y., Huterer D., 2017, MNRAS, 471, 4946
Xiang M., Rix H.-W., Yang H., Liu J., Huang Y., Frankel N., 2025, Nat. Astron., 9, 101

APPENDIX A: LIMITS FROM THE CMB QUADRUPOLE

In addition to the bulk flow curve, another important constraint on any solution to the Hubble tension is its ability to retain consistency with the CMB power spectrum while matching the high local cz'. A local void solution has an advantage in this respect because it does not alter the early universe or the angular diameter distance to the CMB (appendix A of Banik & Kalaitzidis 2025). However, since we cannot be located exactly at the centre of a local void, its potential would gravitationally lens the CMB anisotropically, especially at low multipole moments/large angular scales. The impact on the CMB monopole due to the height of the local potential would be very small (section 5.3.3 of HBK20). Our peculiar velocity creates a dipole in the CMB, which can be explained by the void in about 2 per cent of its volume (see their section 4.2.3).

Given this consistency with the CMB dipole, the impact on higher multipoles would be small according to Alnes & Amarzguioui (2006), whose equations 37–39 'imply that it is impossible to obtain sufficiently large values for the quadrupole and octopole (to significantly affect the observations) as long as the dipole is within the limits set by the data'. They show that the impact on the CMB multipole moment ℓ is $\mathcal{O}\left(\alpha^{\ell}\right)$, where

$$\alpha = \frac{d\left(h_{\rm in} - h_{\rm out}\right)}{3000\,{\rm Mpc}}, \tag{A1}$$

h indicates a value in units of 100 km s^{-1} Mpc^{-1}, $h_{\rm out} = \dot{a}$, $h_{\rm in} = cz'$ within the void, and the constant of 3000 Mpc denotes the Hubble distance $d_H \equiv c/H$ for the case $h = 1$. Any local void solution to the Hubble tension must have $h_{\rm in} - h_{\rm out} \approx 0.07$ (Di Valentino et al. 2025). Since M24 found that we need to be ≈ 150 Mpc from the void centre to match the bulk flow curve, the CMB multipole moments approximately become powers in the parameter $\alpha = 3.5 \times 10^{-3}$, with the quadrupole being $\mathcal{O}\left(\alpha^2\right) \approx 10^{-5}$ and the octopole being $\mathcal{O}\left(\alpha^3\right) \approx 10^{-7}$. It is clear that even if we were to consider substantial changes to our vantage point to account for their mistake with how bulk flows are defined (Section 3.2), the octopole contribution would not be discernible given the extra factor of $\sqrt{16\pi/175} = 0.54$ (equation 39 of Alnes & Amarzguioui 2006), making the void contribution much less than the $\mathcal{O}\left(10^{-5}\right)$ intrinsic octopole in the CMB. Its higher order multipoles would be even less affected by a local void. However, the quadrupole deserves more attention given the comparable magnitudes.

The quadrupole contribution given by equation (38) of Alnes & Amarzguioui (2006) is as follows:

$$a_{20} = \sqrt{\frac{16\pi}{45}}\alpha^2. \tag{A2}$$

Since we will vary the void parameters and our vantage point, we estimate α and thus a_{20} for each combination of parameters. We assume that for a model to be viable,

$$a_{20} < 10^{-5}. \tag{A3}$$

This ensures that the contribution from a local void is smaller than the intrinsic power in the CMB quadrupole. The observed CMB quadrupole must be a combination of the intrinsic quadrupole and *anisotropic* lensing by the potential of any local void the late-time observer might be located within, so too large a contribution from the latter would cause difficulties matching the observed CMB anisotropies. However, even the very extreme void shown in fig. 2 of Nistane, Cusin & Kunz (2019) would only marginally be detectable with *Planck*, highlighting that this argument can only be used to rule out a significant offset from a substantial underdensity. We will see later that despite this limitation, equation (A3) places an important constraint on the allowed solutions. These constraints are significant for the fiducial void size, requiring the observer to be $\lesssim 90$ Mpc from the void centre in all three profiles. We will use this to rule out some solutions in Section B1. On the other hand, the CMB quadrupole constraints become irrelevant for the smaller void sizes preferred by our main field-level analysis, as such voids would not produce any detectable imprint on the CMB for observer locations that plausibly match the local velocity field.

APPENDIX B: FIDUCIAL SIZE RESULTS

B1 Bulk flow constraints

While the main body of this paper focuses on results obtained allowing the void size to vary, here we revisit the fiducial-size models by fixing the size to the values used in HBK20 and varying only the vantage point and external velocity, whose direction is set parallel to the bulk flow of W23. The results of this fixed-size analysis are presented in Fig. B1, where we show that acceptable fits to the W23 bulk flow curve can still be obtained, but only within a narrow range of configurations.

In the left and middle panels of Fig. B1, we show the χ^2 landscape for the exponential and Gaussian profile, respectively. Both profiles give quite similar results. In each case, there are two broad valleys in χ^2. These arise because the bulk flows reported by W23 are actually quite *small* in comparison to the typical peculiar velocity in the void models (see appendix A of M24). Our vantage point needs to be some distance from the void centre so that the void outflow velocity $V_{\rm outflow}$ cancels $V_{\rm ext}$ given these are in opposite directions (in their figures, the void moves to the left and the vantage point is on the right; see also fig. 8 of HBK20). For a given $V_{\rm ext}$, perfect cancellation occurs at some $R_{\rm offset}$. However, we do not want a perfect cancellation because $V_b \neq 0$. Since the orientation of the local void model is not known independently of the observed $\boldsymbol{V}_b$, a good fit to the observed V_b on the smallest probed scales arises when $V_{\rm outflow} - V_{\rm void} = \pm V_b$, though

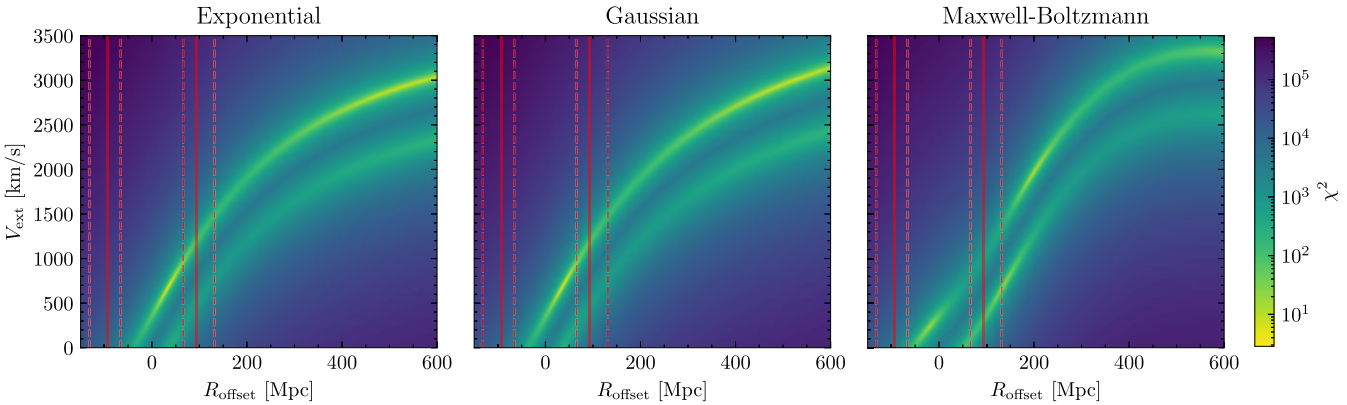

Figure B1. χ^2 as a function of observer offset from the centre of the void ($R_{\rm offset}$) and external velocity magnitude ($V_{\rm ext}$) for exponential, Gaussian, and Maxwell–Boltzmann void profiles (left, middle, and right panel, respectively). The solid vertical lines mark CMB quadrupole consistency limits, while the dashed lines vary the limit on a_{20} by a factor of 2 from the nominal 10^{-5} (see Appendix A). In all three void profiles, the outer solution is excluded, but the inner solutions remain viable.

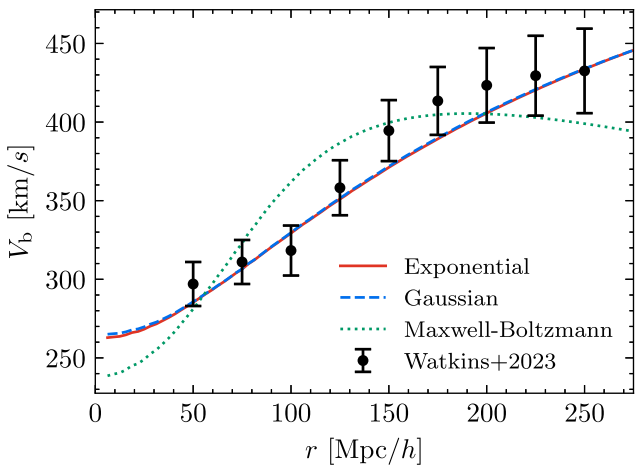

Figure B2. The bulk flow curve for parameters corresponding to the local minima in the χ^2 landscape with acceptable χ^2 for the exponential (red), Gaussian (blue), and Maxwell–Boltzmann (green) void density profile. The plotted curves correspond to the lower $R_{\rm offset}$ (inner) solutions summarized in Table B1.

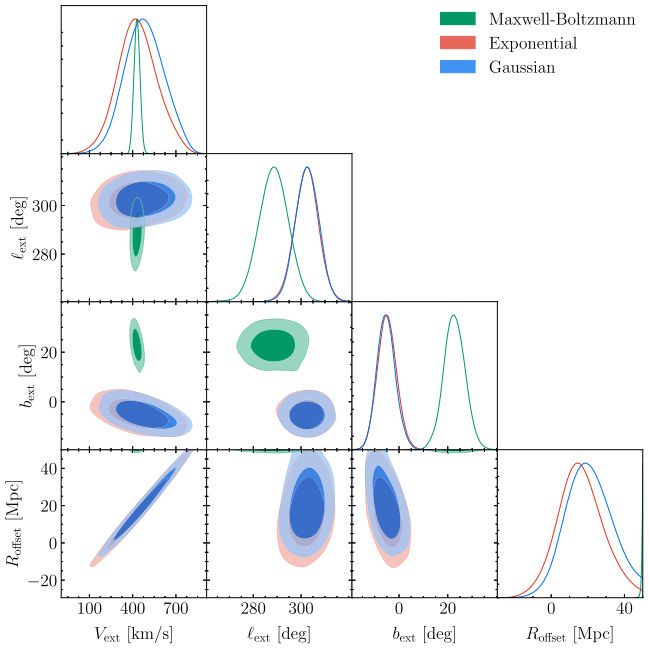

Figure B3. The inferred void model parameters obtained by fitting the flow model described in Section 3.3 to the CF4 data using the *fiducial void size* (HBK20), assuming either an exponential (red), Gaussian (blue), or Maxwell–Boltzmann (green) void profile. An important parameter that we sample is the external velocity, which lies in the direction ($\ell_{\rm ext}$, $b_{\rm ext}$) in Galactic coordinates and has magnitude $V_{\rm ext}$. The other parameter we sample is $R_{\rm offset}$, the distance of our vantage point from the void centre in the direction opposite to $\boldsymbol{V}_{\rm ext}$.

the different signs require opposite relative orientations between $\boldsymbol{V}_b$ and the direction towards the void centre. The + case corresponds to a larger $R_{\rm offset}$ because we expect $V_{\rm outflow}$ to increase with $R_{\rm offset}$ by about 7 km s^{-1} Mpc^{-1} in order to solve the Hubble tension. In both panels, this valley in χ^2 does not contain a viable solution because $\chi^2 \gg 100$. Focusing on the smaller $R_{\rm offset}$ (or upper) valley, we see that there are two viable (bright yellow) regions in the exponential and Gaussian panels of Fig. B1. In principle, both represent viable fits to the bulk flow curve of W23. However, the solution at large $R_{\rm offset}$ places us much too far from the void centre to be consistent with the observed CMB quadrupole. In the following text, we therefore only consider the region towards the lower left in voids with the fiducial size from (HBK20).

In the right panel of Fig. B1, we present the χ^2 landscape for the Maxwell–Boltzmann profile calibrated against the bulk flow curve of W23. Given that there are nine data points and two degrees of freedom, a viable model should ideally achieve $\chi^2 \approx 7$, corresponding to the bright yellow contours. We identify three regions that provide a good fit. The two solutions at $R_{\rm offset} \approx 200$ Mpc imply a substantially off-centre observer, where the CMB quadrupole would experience a significant contribution due to anisotropic lensing by the void (Appendix A). The solid vertical lines indicate the offset at which this contribution reaches 10^{-5}, a rough estimate of the intrinsic quadrupole in the CMB (equation A3). The dashed (dot–dashed) vertical lines represent where the contribution is half (twice) this value. Even allowing for some flexibility in applying the CMB quadrupole constraint, it is clear that both 'outer' solutions are problematic given the excellent agreement of the CMB power spectrum with ΛCDM (Planck Collaboration VI 2020b; Tristram et al. 2024). Furthermore, such a large offset would inevitably introduce significant anisotropy

Table B1. Parameters corresponding to the local minima in the χ^2 landscape with acceptable χ^2 for each density profile. The χ^2 values have been converted to an equivalent tension for a single Gaussian variable assuming seven degrees of freedom, since there are nine data points and we used two free parameters to optimize the fit. The outer solutions are rejected on the basis of the CMB quadrupole constraint (Appendix A), so only the inner solutions shown here are plotted in Fig. B2.

		Density profile		
Quantity	Vantage point	Exponential	Gaussian	Maxwell–Boltzmann
$R_{\rm offset}$ (Mpc)	Inner	36	37	−19
	Outer	538	530	200
$V_{\rm ext}$ (km s^{-1})	Inner	689	699	234
	Outer	2940	3012	1966
χ^2 (tension)	Inner	2.9 (0.13σ)	2.9 (0.13σ)	18.7 (2.61σ)
	Outer	8.6 (1.07σ)	8.6 (1.07σ)	11.4 (1.55σ)

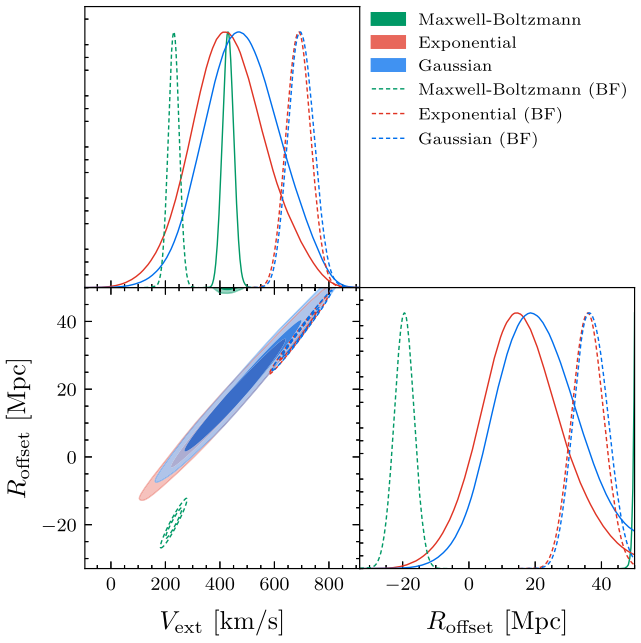

Figure B4. Comparison of $V_{\rm ext}$ and $R_{\rm offset}$ between the field-level (solid) and bulk flow (dashed) constraints for the fiducial void size. The exponential and Gaussian profiles are in good agreement, unlike the Maxwell–Boltzmann profile. It is surprising that the bulk flow curve based on just nine data points gives a much tighter inference.

in galaxy number counts. Given these constraints, we focus only on the 'inner' solution at $R_{\rm offset} \approx -20$ Mpc, where the lensing contribution to the CMB quadrupole would be very small.

To demonstrate that the low χ^2 solutions are indeed good fits to the observed bulk flow curve, we show the predicted bulk flow curve in each case (Fig. B2), with the corresponding parameters summarized in Table B1. Only the inner solution for each profile can be considered viable given the CMB quadrupole constraint (Appendix A), so we only plot the inner solutions in Fig. B2. It is interesting to note that the fiducial void size yields a better fit to the bulk flow curve in terms of χ^2 than the smaller void sizes studied earlier in Section 4.2, where the minimum was $\chi^2 = 9.1$, compared to $\chi^2 = 2.9$ with the fiducial size.

B2 Galaxy-by-galaxy constraints

We now fix the void size to $\tilde{r}_{\rm void} = 1$ and repeat the field-level analysis of the main part of the paper. For a more straightforward comparison to HBK20, we also fix $\beta = 1$. However, we note that these are strong assumptions – in Section 4.1, we have already shown that a value of 1 is not preferred for either parameter. Unlike the bulk flow constraint in Appendix B1, we also treat the direction of $\boldsymbol{V}_{\rm ext}$ in Galactic coordinates ($\ell_{\rm ext}$, $b_{\rm ext}$) as a free parameter.

The inferred values of the void model parameters are shown in Fig. B3. We infer a direction for $\boldsymbol{V}_{\rm ext}$ that is well-aligned with the bulk flow direction reported in table 1 of W23 for both the exponential and Gaussian profile, but not for the Maxwell–Boltzmann profile. The inferred $R_{\rm offset}$ and $V_{\rm ext}$ are highly correlated, which is to be expected given the narrow valleys in the χ^2 landscape evident in Fig. B1. As discussed in Section B1, these valleys arise because of the need for outflow from the void to almost cancel $\boldsymbol{V}_{\rm ext}$ and give a relatively low total $\boldsymbol{V}_{\rm pec}$ at our location, implying a degeneracy between $\boldsymbol{V}_{\rm ext}$ and $R_{\rm offset}$, which sets the outflow velocity.

However, Fig. B4 shows that the best-fitting locations of $V_{\rm ext}$ and $R_{\rm offset}$ differ from the ones inferred by calibrating the void model to the bulk flow curve of W23. In particular, we infer a smaller $R_{\rm offset}$ and correspondingly smaller $V_{\rm ext}$. Even so, the tension between the field-level and bulk-flow-only constraint is 1.7σ (1.6σ) for the exponential (Gaussian) profile, suggesting no strong disagreement. As with the varying void size analysis, it is surprising that the uncertainties from the bulk flow constraint are significantly tighter than those from the field-level inference, despite the latter having in principle access to more information than the single summary statistic of the bulk flow. This likely reflects either an underestimation of the bulk flow uncertainties (Whitford et al. 2023) or the neglect of correlations between the bulk flow measurements when fitting the void model. In contrast, the field-level analysis for the Maxwell–Boltzmann profile indicates $R_{\rm offset} > 50$ Mpc and $V_{\rm ext} > 400$ km s^{-1}, in tension with the bulk flow constraints as these favour $R_{\rm offset} \approx -19$ Mpc and $V_{\rm ext} \approx 234$ km s^{-1}.

Upon comparing the Bayesian evidence across the three fiducial void profiles, we find that the Maxwell–Boltzmann model is strongly disfavoured. The exponential and Gaussian profiles yield $\log \mathcal{B}$ values of 83.5 and 83.0, respectively, relative to the Maxwell–Boltzmann case. Given this decisive evidence, the fiducial Maxwell–Boltzmann profile is ruled out by the CF4 data and is not considered further in this analysis. These results are consistent with the bulk flow-only analysis, which cannot distinguish between the exponential and Gaussian profiles, but yields a χ^2 value worse by 15.8 for the Maxwell–Boltzmann profile (see also M24).

Having inferred $\boldsymbol{V}_{\rm ext}$ and $R_{\rm offset}$, we now show the void density profile, outflow velocity curve, and bulk flow curve in Fig. B5. Its left panel shows the expected 20 per cent underdensity at the void centre for the exponential and Gaussian profiles. The density rises towards the cosmic mean further out, but only gradually, since the fiducial void size is 1030 cMpc. On the other hand, the Maxwell–Boltzmann

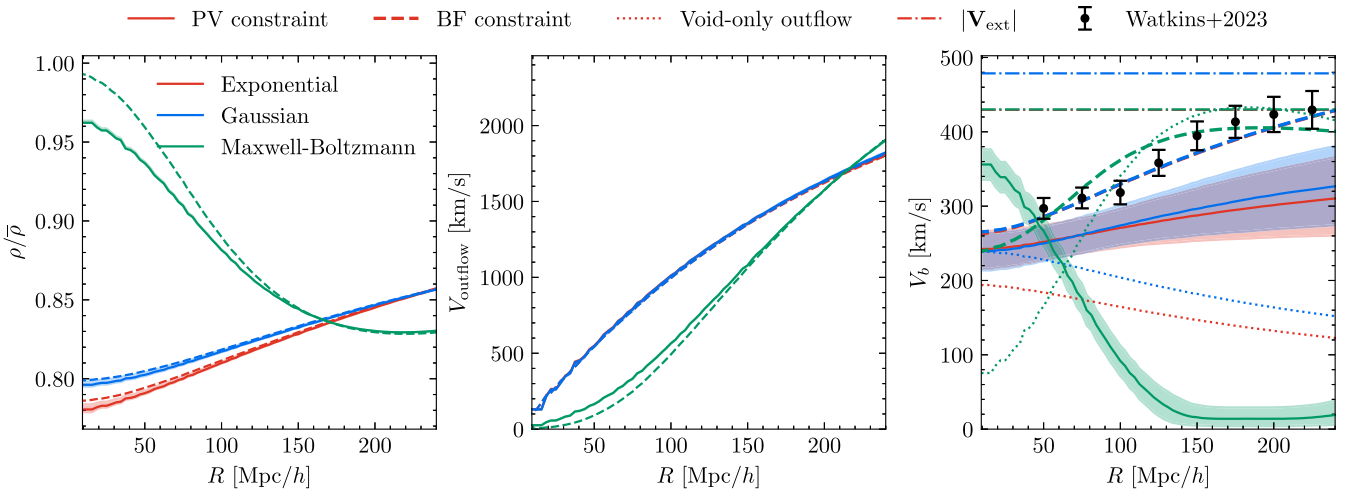

Figure B5. The inferred density field of the *fiducial size* void (left panel), the outflow velocity curve from the void centre (middle panel), and the bulk flow curve (right panel), using the void parameters and their uncertainties as inferred by our flow analysis. We show results for the exponential (Gaussian; Maxwell–Boltzmann) profile using red (blue; green) shaded bands, which indicate the 1σ uncertainty. In the right panel, the dot–dashed lines show $V_{\rm ext}$ (the exponential and Gaussian profile curves overlap) and the dotted lines show the bulk flow without considering $\boldsymbol{V}_{\rm ext}$, illustrating its impact. The dashed lines show the bulk flow curve in the model that best fits that reported by W23, which we show as black points with uncertainties.

profile exhibits a growing underdensity out to $\approx 200\,{\rm Mpc}\,h^{-1}$, after which the void gradually becomes shallower and approaches the cosmic mean density. The middle panel shows that the outflow velocity at first rises with a rate of $\approx 10\ {\rm km\,s^{-1}\,Mpc^{-1}}$, before gradually becoming less steep as the density gets closer to the cosmic mean. At the void centre, we expect the outflow velocity to rise somewhat faster than the magnitude of the Hubble tension ($cz' - \dot{a}$) because the observed cz' is an average over a large range of radii, reducing the average value compared to that at the void centre. The right panel shows that our analysis prefers exponential and Gaussian models where the bulk flow curve rises less steeply than reported by W23. This is related to the fact that our field-level analysis places us closer to the void centre, where the bulk flow curve would be nearly flat. The dotted curves, which show the void-only outflow, highlight that the bulk flow in these models is largely due to $\boldsymbol{V}_{\rm ext}$, since removing it leads to only a very small V_b. However, $\boldsymbol{V}_b$ does not entirely arise from $\boldsymbol{V}_{\rm ext}$ either – if it did, we would get $\boldsymbol{V}_b = \boldsymbol{V}_{\rm ext}$ at all radii, leading to a flat bulk flow curve. The dashed lines provide a check of our earlier result that the predicted bulk flow curve in any of the considered void profiles can provide a good match to that reported by W23, if the void model is calibrated to it. The bulk flow curves inferred by our field-level analysis provide a reasonably good match to that reported by W23 for the exponential and Gaussian profiles, though the W23 result rises a bit more steeply. On the other hand, in the case of the Maxwell–Boltzmann profile, $\boldsymbol{V}_{\rm ext}$ cancels the void outflow at large radii according to our field-level analysis, leading to a negligible bulk flow. This is strongly incompatible with W23, and indeed the fiducial Maxwell–Boltzmann void is strongly rejected by our model comparison metric.

This paper has been typeset from a TEX/LATEX file prepared by the author.